Minimum heat flow from the core and thermal evolution of the Earth

V. Patočka[a,b,*], O. Šrámek[b], N. Tosi[a,c]

[a] *Institute for Planetary Research, German Aerospace Center (DLR), Berlin, Germany*
[b] *Department of Geophysics, Faculty of Mathematics and Physics, Charles University, Prague, Czech Republic*
[c] *Department of Astronomy and Astrophysics, Technische Universität, Berlin, Germany*

ABSTRACT

The role of heat flow coming from the core is often overlooked or underestimated in simple models of Earth's thermal evolution. Throughout most of Earth's history, the mantle must have been extracting from the core at least the amount of heat that is required to operate the geodynamo. In view of recent laboratory measurements and theoretical calculations indicating a higher thermal conductivity of iron than previously thought, the above constraint has important implications for the thermal history of the Earth's mantle. In this work we construct a paramaterized mantle convection model that treats both the top and the core-mantle boundary heat fluxes according to the boundary layer theory, or alternatively employs the model of Labrosse (2015) to compute the thermal evolution of the Earth's core. We show that the core is likely to provide all the missing heat that is necessary in order to avoid the so-called "thermal catastrophe" of the mantle. Moreover, by analyzing the mutual feedback between the core and the mantle, we provide the necessary ingredients for obtaining thermal histories that are consistent with the petrological record and have reasonable initial conditions. These include a sufficiently high viscosity contrast between the lower and upper mantle, whose exact value is sensitive to the activation energy that governs the temperature dependence of the viscosity.

1. Introduction

The secular loss of heat from the deep Earth is reasonably well constrained by land and sea-floor heat flow measurements (e.g. Jaupart et al., 2015). Much more uncertainty remains in the attempt to separate the total surface heat loss into the two major contributions, the secular cooling and ongoing differentiation (inner core growth) of the planet on one hand, and the power of radiogenic heat sources (radionuclides of U, Th, K) on the other. Our current understanding offers a rather accurate estimate of radiogenic heat production in the Earth's crust, and argues for negligible to very limited radiogenic power in the Earth's core. The question thus remains how much radiogenic power is available in the convecting mantle. Typically, cosmochemical and geochemical estimates result in smaller values compared to what most geophysical models require (e.g. Korenaga, 2008). Here we explore one possible solution to this discrepancy – while aware of the several other ways out of this conundrum proposed by other authors.

As the concept of mantle convection in the Earth started to be widely accepted in the 1970s, investigating the heat loss of a convecting system was gaining increasing attention. Both experimental (Rossby, 1969; Booker and Stengel, 1978) and numerical (McKenzie et al., 1974; Young, 1974)) studies found the surface heat flux and the temperature

difference across a convecting layer of fluid to be related via $Nu \propto Ra^{\beta}$ scaling, where the Nusselt number Nu is a measure of the surface heat flux, the Rayleigh number Ra is a measure of the convective vigour of the system, and the exponent β is equal to 1/3. This relationship was found to hold for a broad variety of convective regimes: for basally heated convection, internally heated convection (Schubert et al., 1979), and for convection of non-Newtonian fluids (Parmentier et al., 1976). However, the exact value of the exponent β may differ from 1/3. Theoretically, the scaling law is supported by boundary layer theory (Turcotte and Oxburgh, 1967). Both the transient and steady state boundary layer theories predict the same value of β and differ only in the constant of proportionality (e.g., chapters 6.20 and 6.21 in Turcotte and Schubert, 2002).

Already the earliest works that studied Earth's thermal evolution with the help of the $Nu - Ra$ scaling provided constraints on the amount of radiogenic heating in the mantle. The ratio of heat production within the convecting mantle over the total convective heat flow is referred to as convective Urey ratio (Ur) (Christensen, 1985). Schubert et al. (1980) showed that the Urey ratio must be smaller than 1, because secular cooling also contributes to the present-day heat flow. The authors investigated a broad range of model parameters and demonstrated that the Urey ratio is likely to be smaller than ≈ 0.8, which corresponds

---

* Corresponding autor at: Institute for Planetary Research, German Aerospace Center (DLR), Berlin, Germany.
E-mail address: patocka.vojtech@gmail.com (V. Patočka).

to secular cooling being responsible for at least 20% of the present-day surface heat flow. Davies (1980), on the other hand, argued that the Urey ratio must be greater than ≈ 0.7 because smaller values would result in an extremely hot mantle in the past. However, such high values imply that the radiogenic power in the mantle is larger than what is suggested by most geochemical estimates of the Bulk Silicate Earth (BSE) composition, which imply a Urey ratio of ≈ 0.2–0.3 (e.g., Table 2 in Bellini et al., 2013 and references therein, or Tables 9 and 12 in Jaupart et al., 2015, from which we show an excerpt here in Table 2). In other words, based on estimates from cosmochemistry and geochemistry, one would obtain an extremely hot mantle in relatively recent geological history, a paradox known as "thermal catastrophe".

One attempt to avoid the thermal catastrophe was considering mantle convection to be layered in the past (e.g., Yuen et al., 1994; Honda, 1995). Butler and Peltier (2002) showed that a gradual transition from layered to whole-mantle convection could result in avoiding the thermal runaway. Later, however, experimental studies indicated that the negative Clapeyron slope of the endothermic phase change is smaller in magnitude than previously thought (Katsura et al., 2003), making such a scenario less dynamically feasible. Moreover, the above studies overemphasize the role of the endothermic phase change as they do not account for large and stiff plates, which tend to promote whole mantle convection (Tackley, 1995; Korenaga, 2008). Convincing evidence against the layering of present-day mantle convection is provided by seismic tomography (e.g., Megnin et al., 1997; van der Meer et al., 2010).

The thermal catastrophe is a consequence of the strong temperature dependence of the conventional scaling law, often referred to as the Tozer effect (see Tozer, 1965; Christensen, 1985). Another possibility to avoid the thermal runaway is thus to lower this temperature dependence or to move beyond the conventional *Nu–Ra* scaling. Solomatov (2001) suggested that the grain-growth kinetics may reduce or even reverse the temperature dependence. He argued that a hotter mantle may become stiffer because it would contain larger mineral grains, effectively increasing the mantle viscosity. The grain-growth kinetics and its interaction with convective deformation is, however, still poorly understood (Bercovici and Ricard, 2005). Conrad and Hager (1999) rejected the conventional scaling on the basis that the rate at which the Earth loses heat is controlled by the resistance of subducting plates towards bending, and proposed a temperature independent scaling. Sleep (2000) and Korenaga (2003) further explored this idea and suggested that higher temperatures in the past may in fact imply lower heat loss through the Earth's surface. This is because a hotter mantle starts to melt at a greater depth, which results in a thicker depleted lithosphere and thus thicker plates that are more difficult to bend and subduct. Korenaga (2010) investigated the scaling of plate-tectonics in a 2–D numerical study, observing the scaling to be only mildly temperature-dependent (see also a review by Korenaga, 2013).

However, Davies (2009) argued that the effect described above may only be significant at rather extreme conditions confined to Earth's early history. The scalings proposed by Conrad and Hager (1999) and Korenaga (2003) assume a constant slab bending radius, whereas in reality the bending radius adjusts according to the slab thickness, strength, and buoyancy. Convection models with temperature-dependent viscosity and pseudo-plastic yielding in the plate-like regime also follow the classical $Nu \propto Ra^{\frac{1}{3}}$ scaling (Grigne et al., 2005). In this study we adhere to $Nu \propto Ra^{\frac{1}{3}}$, which is supported by theory and numerical experiments (e.g. Turcotte and Oxburgh, 1967; Jarvis, 1984; Schubert and Anderson, 1985). To account for the possibility of a scaling with milder temperature dependence we investigate also a scenario with $\beta = 0.27$, which can be considered as an end-member of a particular class of admissible scalings (see Section 2 for details).

Crowley et al. (2011) constructed a model of convecting mantle which can degas (specifically, lose hydrogen) at mid-oceanic ridges and re-gas (gain hydrogen) at subduction zones. When they include the

dynamic feedback from viscosity, which is not only temperature-dependent, but also depends on hydrogen content, the Urey ratio shifts to lower values, lowering the discrepancy between the geochemical and the geophysical models in effect.

Noteworthy is also the work of Höink and Lenardic (2010), who find two distinct flow types in the asthenosphere. Below small lithospheric plates, the plate-bending resistance exceeds viscous dissipation in the asthenosphere, resulting in channelized Poiseuille flow with velocities larger than those of the surface plate ("asthenosphere drive"). Below large plates, on the other hand, asthenospheric flow is driven by the horizontal motion of the overlying plate, resulting in Couette flow ("slab-pull"). These two regimes yield a different heat loss scaling and Höink et al. (2013) then speculate that cooling of the Earth is a superposition of the two. Since the heat loss corresponding to asthenosphere drive is only mildly dependent on internal temperature, thermal evolution models can be constructed that avoid the thermal catastrophe if the relative contribution of this regime is sufficiently large (roughly 65%). Yet, the numerical simulations of Höink and Lenardic (2010) do not account for elasticity and a free surface, and their overlying plate subducts in the corner of their Cartesian box. These model assumptions may play a significant role in determining the plate-bending resistance (Patočka et al., 2018). In the present work, we do not account for multiple convection modes: our aim is to investigate to which extent the classic scaling, i.e. long-wavelength convection with the heat transfer dominated by sinking plates, is capable of reconciling the available constraints on Earth's thermal evolution.

In earlier studies that used parametrized convection to constrain the amount of radiogenic heat in the mantle, the heat flow from the Earth's core was considered unimportant. Schubert et al. (1980) and Davies (1980) assumed a thermally insulating core–mantle boundary. Core heat was also neglected by Crowley et al. (2011). In Höink et al. (2013), core heat is neglected when solving the energy balance (see their Eq. (1)), and then estimated only a posteriori as shown in their Fig. 2 (Adrian Lenardic, personal communication). In the review by Korenaga (2013), the thermal evolution is computed for the Earth as a whole, representing the mantle and core using a single average temperature. This approach, however, implicitly treats the core in a simplified manner, as it assumes that the secular cooling rate of the mantle equals that of the core, which is unlikely (Jaupart et al., 2015). This alone calls for a better treatment of the core heat flow in parametrized convection models. The heat flow from Earth's core is certainly not negligible: the core must have cooled by hundreds of degrees since its formation and sustained the operation of the geodynamo for most of its history (e.g., Mollett, 1984; Grigné and Labrosse, 2001; Jaupart et al., 2015).

Despite the fundamental importance of the thermal conductivity of high-pressure iron for geodynamo considerations and for the nucleation and growth of the inner core, the value of this parameter remains controversial (see review by Williams, 2018). Recent experimental measurements and theoretical calculations point either to relatively low values (≈ 30 W/m/K according to Konôpková et al., 2016), in line with older predictions (Stacey and Anderson, 2001), or to high values (≈ 90 W/m/K), which seem to be favored across different groups (de Koker et al., 2012; Pozzo et al., 2012; Gomi et al., 2013; Ohta et al., 2016). A high thermal conductivity of the core has important implications for the minimum amount of heat that the mantle must extract in order to sustain a magnetic dynamo in the outer core (Davies, 2015; Labrosse, 2015). In a recent summary, Labrosse (2016) suggested that a high value of the core-mantle heat flow could help solve the "thermal catastrophe": When assuming a high heat flow from the core, the amount of radiogenic power in the mantle does not have to be high and it is possible to obtain a reasonably slow secular cooling of the mantle. Indeed, this effect was already reported by Driscoll and Bercovici (2014), who focused on the effects of including melting into parametrized thermal history models. Driscoll and Bercovici (2014) calculated the core-mantle boundary (CMB) heat flux based on the same scaling adopted to treat the surface thermal boundary layer and checked a

posteriori whether their models were capable of generating a dynamo.

Here, we use a different approach. In the first part of our study, we prescribe the CMB heat flow such as to always generate the geodynamo and systematically explore scenarios for Earth's thermal evolution. To this end, we couple a conventional parametrized convection model of the Earth's mantle with the recent model of Earth's core evolution by Labrosse (2015). His use of a high-order polynomial approximation for the core density profile has changed the estimate of the temperature gradient at the top of the core by about 30% relative to the previous simpler parametrizations. By setting the CMB heat flow to the minimum value required to sustain the geodynamo, we find the upper limit of radiogenic power in the mantle that is consistent with present-day observations of surface heat flow and mantle potential temperature.

In Section 4, we employ a similar approach as Driscoll and Bercovici (2014) and assume a parametrization for both the top and bottom thermal boundary layers. Unlike in their study, we focus on the shape of thermal history solutions and compare our simulations with the petrological record of the Earth's mantle. The data set of Herzberg et al. (2010), consisting of source temperatures inferred for non-arc Archean and Proterozoic basalts, is used for this purpose. We discuss the role of the viscosity contrast between the lower and upper mantle and show that, for small to intermediate viscosity contrasts, the mantle temperature is always expected to reach peak values in the Archean, but that the resulting thermal histories have unrealistically low initial mantle temperatures. For high viscosity contrasts, on the other hand, the dynamo constraint is violated. The range of physically acceptable parameters over which our parametrized model satisfies the observational constraints is rather narrow, but not void, and as such, the classical Nu–Ra scaling cannot be rejected on the grounds of yielding implausible Earth's thermal histories.

2. Parametrized model of mantle convection

2.1. Governing equations

The temperature of the mantle evolves according to the equation

$$C_m \frac{dT_m}{dt} = H + Q_{CMB} - Q_S, \tag{1}$$

where C_m is the effective heat capacity of the mantle, T_m the mantle potential temperature, H the radiogenic power in the mantle, Q_{CMB} the heat flow from the core, and Q_S the surface heat flow (e.g., Jaupart et al., 2015).

Radionuclides of uranium (^{238}U, ^{235}U), thorium (^{232}Th), and potassium (^{40}K) account for > 99% of present-day radiogenic power:

$$H(t) = \sum_i H_i^0 \exp\left(\frac{-t \log 2}{\tau_{1/2}^i}\right) \tag{2}$$

where H_i^0 is the radiogenic power from radionuclide i at time $t = 0$. With the exception of the models presented in Section 2.2, we integrate Eq. (1) backward in time, setting $t = 0$ at present and $t < 0$ in the past. The value of present-day radiogenic power $H_0 = \Sigma_i H_i^0$ is being systematically varied without changing the relative proportions of present-day radionuclide abundances. Model parameters are listed in Table 1.

The heat flow from the core, Q_{CMB}, is discussed in Section 3. Until then, we neglect it and set its value to zero, as was done in the early works of Schubert et al. (1980) and Davies (1980), as well as in more recent ones such as Crowley et al. (2011). The convective heat flow Q_S represents the amount of heat loss through the Earth's surface due to mantle convection, and excludes radiogenic heat generated in the crust (i.e., non-convecting surface layer). It can be shown to scale with the Rayleigh number Ra as (e.g., Sotin and Labrosse, 1999)

$$Q_S = AS_m \frac{k(T_m - T_s)}{D} Ra^\beta \left(\frac{T_m}{T_m - T_s}\right)^{1+\beta}, \tag{3}$$

Table 1
Model parameters.

Parameter	Symbol	Value	Units
Present-day convective heat flow[1]	Q_S^0	38	TW
Present-day potential temperature[2]	T_m^0	1680	K
Surface temperature	T_{surf}	293	K
Activation energy[3]	E_{act}	300	kJ/mol
Gas constant	R	8.314	J/mol/K
Heat capacity of the mantle[4]	C_m	7×10^{27}	J/K
$H_{U238}^0/H_{U235}^0/H_{Th232}^0/H_{K40}^0$[5]		1/0.0429/1.0472/0.5039	

[1,2]Jaupart et al. (2015), [3]Driscoll and Bercovici (2014), [4]Stacey (1981), [5]McDonough et al. (2019).

where A is a dimensionless coefficient, S_m is the surface area of the Earth's mantle, k is the mantle thermal conductivity, D is the mantle depth, and T_s is the surface temperature. The Rayleigh number is defined as

$$Ra = \frac{g\alpha(T_m - T_s)D^3}{\kappa\nu}, \tag{4}$$

where g is the gravitational acceleration, α the thermal expansivity, and κ the thermal diffusivity. The effective kinematic viscosity ν is assumed to be strongly temperature dependent:

$$\nu = \nu_0 \exp\left(\frac{E_{act}}{RT_m}\right), \tag{5}$$

where R is the gas constant, E_{act} is the activation energy, and ν_0 is the reference viscosity. Since the present-day convective heat flow and present-day mantle temperature are relatively well known, we can use these values to eliminate A, S_m, k, D, g, α, κ, and ν_0 in the scaling law and rewrite Eq. (3) as (e.g., Labrosse, 2016):

$$Q_S = Q_S^0 \left(\frac{\nu(T_m)}{\nu(T_m^0)}\right)^{-\beta} \left(\frac{T_m}{T_m^0}\right)^{1+\beta}. \tag{6}$$

We choose the values of the present-day convective heat flow Q_S^0 and present-day mantle potential temperature T_m^0 to be 38 TW and 1680 K respectively (Jaupart et al., 2015, see also Table 2 here).

With Q_{CMB} set to zero, Eqs. (1), (2), and (6) form an ordinary differential equation (ODE) that can be numerically integrated backward in time. The key parameters controlling the behavior of its solution are the exponent β and the activation energy E_{act}.

The exponent β in Eq. (3) is typically found to be close to 1/3. Note that for $\beta = 1/3$ the heat flow is independent of the thickness of the whole mantle, D. This can be expected for convection at a high Rayleigh number, as the heat loss is controlled by processes happening in a thin boundary layer near its surface (e.g., Labrosse, 2016).

Most of the earlier theoretical work mentioned above considered isoviscous convection, that is, the viscosity was spatially uniform in the respective models. The viscosity was assumed to depend on a single temperature T_m, representing the entire mantle, and could evolve with time as a model cooled down or heated up. When the temperature dependence of the viscosity is taken into account in the modelling of mantle flow itself (i.e. the viscosity varies spatially in the model

Table 2
Mantle energy budget - excerpt from a review by Jaupart et al. (2015).

Quantity	Preferred value	Range
Total surface heat loss	46 TW	43–49 TW
Continental heat production (crust + lith. mantle)	8 TW	7–8 TW
Heat flow from convecting mantle	38 TW	35–41 TW
Radioactive heat sources (convecting mantle)	11 TW	9–17 TW
Present Urey ratio	0.29	0.12–0.49
Heat from core	11 TW	5–17 TW

because also the temperature does), a stagnant lid regime is obtained (e.g. Moresi and Solomatov, 1995). For stagnant lid convection, one can still apply the $Nu \propto Ra^\beta$ scaling, but with Ra replaced by an effective Rayleigh number accounting for the effective viscosity of the convective sublayer beneath the stagnant lid, and β that typically takes a lower value ranging from 0.2 as predicted by boundary layer theories (e.g. Fowler, 1993; Reese et al., 1998), to about 0.27 as determined from numerical experiments (e.g. Deschamps and Lin, 2014).

It was shown by Gurnis (1989) and Honda (1997), that when a weak zone is introduced within the lithosphere in order to split the lid into multiple plates in the models of temperature-dependent viscosity convection, the conventional ("isoviscous") $Nu \propto Ra^{\frac{1}{3}}$ scaling is again recovered. For this reason we investigate two values of β here. First, we set $\beta = 1/3$ to represent the conventional scaling. Second, we set $\beta = 0.27$ to represent a low-β end-member of a particular class of temperature-dependent scalings, as this value was obtained for stagnant lid convection by Deschamps and Lin (2014).

2.2. Transition solution

First, we briefly repeat the analysis of Davies (1980) to demonstrate the mathematical nature of the problem. In Fig. 1 we integrate the governing equations backward in time varying H_0 evenly between 0 and 38 TW (i.e., Urey ratio, H_0/Q_S^0, goes from 0 to 1). The heat flow from the core, Q_{CMB}, is set to zero. Each line represents a solution of the system of Eqs. (1), (2), and (6) for a particular value of H_0. Due to the strong temperature dependence of the heat flow, the range of H_0 for which the surface heat flow Q_S is neither too high nor too low throughout Earth's history is extremely narrow.

Choosing $H_0 \leq 28.50$ TW results in temperatures exceeding tens of thousands of degrees (and thus enormous surface heat flows) at time $t = -4.5$ Gyr, while for $H_0 \geq 29.26$ TW the heat flow Q_S is close to zero TW at $t = -4.5$ Gyr. This implies that the transition between "hot" and "cold" thermal histories is very sharp in terms of the range of H_0. In fact, we can consider the transition range of H_0 to be a single value, denoted as H_0^*. Regardless of the exact definition of "hot" vs "cold" histories, for values of H_0 that are outside the $H_0^* \pm 1\%$ range, the surface heat flow is either thousands of TW or only a few TW at time $t = -4.5$ Gyr (Fig. 1).

Here we define the transition value H_0^* as the smallest value of H_0

for which the mantle potential temperature $T_m(-4.5 \text{ Gyr})$ is equal to, or smaller than 1800 K, which roughly corresponds to the rheological transition during the crystallization of Earth's primordial magma ocean (Litasov and Ohtani, 2002). Given that other parameters are fixed, we label $H_0^* = H_0^*(T_m^0, Q_S^0)$ the function that marks the transition value H_0^* for a given Q_S^0 and T_m^0, and the respective thermal history, $T_m(t)$, is referred to as the "transition solution" (cf. the black line in Fig. 1, obtained by using finer sampling of the solutions than the one depicted).

Since the geological record implies that during Earth's thermal history the mantle temperature was, at least to the Hadean eon, low enough to keep most of the mantle solid and high enough for mantle convection to operate, the present-day H_0 can be expected to be close to the transition value H_0^* (e.g., Davies, 1980). Note that while the solutions in Fig. 1 evenly sample the range from 0 to 38 TW, line spacing is very sparse near H_0^* and becomes dense only at the edges where the Urey ratio is 0 or 1, confirming the robustness of the above statement.

In the vicinity of the transition value H_0^*, the computed solutions are typically not monotonic. It was argued by Korenaga (2013) that the petrological data in Herzberg et al. (2010) suggest that around 3 Gyr ago the average temperature of the mantle reached a maximum, in contrast with results from conventional parametrized models that supposedly predict the mantle temperature to always be convex (with the temperature always increasing to the past). However, close to the transition value H_0^*, we obtain a non-monotonic solution, with a maximum around -3.8 Gyr (cf. the black line in Fig. 1: the solution is concave from -4.5 Gyr to ca. -3 Gyr and only then it is convex until the present-day). As already outlined above and discussed further below, the present-day H_0 must be close to the transition value given by the function $H_0^*(T_m^0, Q_S^0)$, with T_m^0, Q_S^0 given by present-day observations. In general, conventional parametrized models do not necessarily predict a monotonic thermal history (cf. also the mantle temperature evolution in Labrosse and Jaupart, 2007).

It is illustrative to integrate the governing equations forward in time for a fixed value of H_0, varying only the initial temperature $T_m(-4.5 \text{ Gyr})$. In Fig. 2 we perform several integrations forward in time, evenly varying the initial temperature from 1200 to 4200 K and keeping H_0 fixed at 17 TW, which is the upper bound of the 9–17 TW range given by Jaupart et al. (2015). After a certain time, usually termed "mantle adjustment time", the $Q_S(t)$ curve starts to follow the $H(t)$ curve regardless of the initial mantle temperature. Both curves acquire a similar shape, that is, their time derivatives begin to match, while they keep being separated from each other by a rather constant
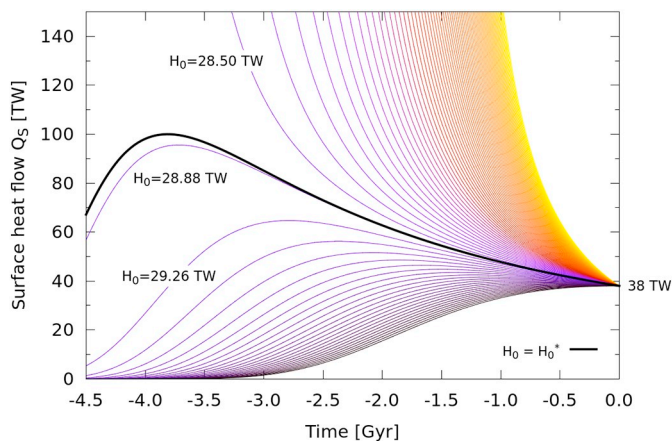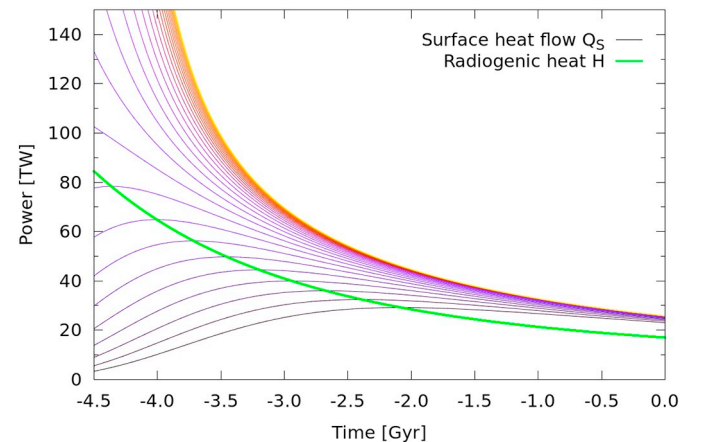

Fig. 1. Backward-in-time integration of the governing equations. The solutions correspond to 100 evenly sampled values H_0 (the present-day radiogenic power). We show the temporal evolution of the surface heat flow Q_S, where colour distinguishes the different solutions: yellow refers to the "hot" end of the spectrum, with $Ur = 0$ ($H_0 = 0$ TW), while black to the "cold" end with $Ur = 1$ ($H_0 = 38$ TW). For $H_0 = 28.86$ TW, i.e. for Urey ratio H_0/Q_S^0 close to 0.76, the transition solution is reached (black line). (For interpretation of the references to colour in this figure legend, the reader is referred to the web version of this article.)

Fig. 2. Forward-in-time integration of the governing equations. The radiogenic power $H(t)$ (green curve) follows Eq. (2) with $H_0 = 17$ TW. The remaining lines show the surface heat flow Q_S, where the colour corresponds to the initial mantle temperature: 30 solutions are evenly sampled from 1300 K (black) to 4300 K (yellow). All the forward integrations converge to ca. 25 TW, making the present-day Urey ratio ≈ 0.7. (For interpretation of the references to colour in this figure legend, the reader is referred to the web version of this article.)

gap – this represents the secular cooling of the mantle. The rate of the secular cooling, that is, the amplitude of the gap between $Q_S(t)$ and $H(t)$, is controlled primarily by the activation energy E_{act}. From Fig. 2 one can also see that for the "hot" histories, the mantle adjustment time is much smaller than the age of the Earth, while for "cold" histories the two timescales are comparable.

As explained by Davies (1980), the condition $\frac{dQ_S(t)}{dt} = \frac{dH(t)}{dt}$ is a defining feature of the transition solution and thus, as long as the initial mantle temperature is within a reasonable range, one converges to the transition solution at some point (when naturally proceeding forward in time). In other words, the present-day amount of radiogenic heat H_0 must be close to $H_0^*(T_m^0, Q_S^0)$. The tendency of the solution to converge to a constant Urey ratio has also been shown analytically (Christensen, 1985; Labrosse and Jaupart, 2007). This, of course, is valid only under the assumption that the scaling law (3) applies to the Earth, when looked from present to the past, for a period of time longer than the mantle adjustment time. Note, however, that the Earth's mantle was likely hotter in the past, making the mantle adjustment time rather small.

Even though $H_0 = 17$ TW in the mantle is on the upper limit of the geochemical BSE estimates, the present-day surface heat flow Q_S converges to ca. 25 TW in Fig. 2, a much smaller value than the observed 38 TW (Table 2). This is an expression of the thermal catastrophe discussed above, now from the viewpoint of time forward integration. It implies that a heat source is missing in the above calculations. In the rest of the paper we analyze whether the core–mantle boundary can provide the missing heat.

We stress that forward-in-time vs backward-in-time integrations are just two mathematical approaches to solving one set of equations. As such, both approaches are in principal equivalent and yield, for a given set of parameters, identical solutions. For a given time window $\langle t_{min}, t_{max} \rangle$, any existing solution of the governing Eqs. (1),(2),(5), and (6) can be obtained by either forward or backward integration. Close to the transition solution, however, large variations of T_m at time $t = -4.5$ Gyr are reached when changing H_0 or $T_m(t=0)$ by only small amounts. While Fig. 1 illustrates the sensitivity to changes in H_0, Fig. 2 illustrates a similar effect in terms of changes in $T_m(t=0)$: the figure can be reproduced also via backward integration by keeping $H_0 = 17$ TW and varying the boundary condition, $T_m(t=0)$, according to the values resulting from the forward simulations (spanning only ca. 30 K for all the depicted solutions). This sensitivity of backward in time integration to the boundary conditions is sometimes used to argue against using the method in the first place, by saying that the obtained solution is not robust, while forward in time integrated solutions are typically robust. As long as the backward in time integration is used for determining the heat source history $H(t)$ (resp. $H(t) + Q_{CMB}(t)$) that is consistent with present-day observations of the surface heat flow Q_S^0, both approaches are equivalent tools for analyzing the Earth's thermal history.

3. Evolution of the core: sustaining earth's dynamo

3.1. Governing equations

In this section we briefly introduce the model of the Earth's core by Labrosse (2015), in order to reconstruct the minimum heat flow from the core that is required to sustain the Earth's dynamo. We adopt all model parameters from Labrosse (2015). The most important one is the thermal conductivity of iron at high pressure and temperature, which recent laboratory measurements and theoretical ab-initio calculations predict to be around 90 W/m/K (de Koker et al., 2012; Pozzo et al., 2012; Ohta et al., 2016), that is, a factor 2 to 3 higher than previous estimates (e.g. Stacey and Anderson, 2001).

The density of the core ρ_a is obtained by solving the Adams-Williamson equation, resulting in the following expression

$$\rho_a = \rho_0 \left(1 - \frac{r^2}{L_\rho^2} - A_\rho \frac{r^4}{L_\rho^4} \right), \tag{7}$$

which is accurate to the 4-th order in r/L_ρ. As explained in Labrosse (2015), a high-order polynomial is necessary to capture the temperature gradient near the CMB correctly and differs from previous models by up to tens of percent in the estimates of the heat flux conducted along the adiabat. The central value ρ_0 is equal to 12451 kg/m³, r is the radius, $L_\rho = 8039$ km, and $A_\rho = 0.484$. The temperature is assumed to be isentropic in the core because it is vigorously convecting. For a constant Gruneisen parameter $\gamma = 1.5$, the temperature T_a then follows the relation

$$T_a(r, r_{IC}) = T_L(r_{IC}) \left(\frac{\rho_a(r)}{\rho_a(r_{IC})} \right)^\gamma, \tag{8}$$

where r_{IC} is the radius of the inner core boundary, and T_L is the pressure and composition dependent liquidus temperature. Prior to the onset of inner core crystallization, Eq. (8) reduces to $T_a(r) = T_0(\rho_a(r)/\rho_0)^\gamma$, with T_0 being the central value. The temperature of the liquidus T_L can be expressed as a function of the radius of the inner core (Labrosse, 2015),

$$T_L(r_{IC}) = T_{L0} - K_0 \left(\frac{\partial T_L}{\partial P} \right)_\xi \frac{r_{IC}^2}{L_\rho^2} + \left(\frac{\partial T_L}{\partial \xi} \right)_P \frac{\xi_0}{f_C(r_C, 0)} \frac{r_{IC}^3}{L_\rho^3}, \tag{9}$$

where r_C is the radius of the core and ξ is the mass fraction of a fictitious, perfectly incompatible light element that is driving compositional convection in the outer core during the crystallization of the inner core (IC) (Labrosse, 2015). This element represents all the likely light elements in the core: e.g. O, S, and Si (Poirier, 1994). The partial derivative of the liquidus with respect to pressure is set to 9 K/GPa, and the partial derivative with respect to mass fraction of the light element is -21×10^3 K. The central value of the temperature of the core at the onset of IC crystallization, T_{L0}, is 5840 K. The mass fraction of the light element prior to the freezing of the inner core, ξ_0, is 5.34%. The auxiliary function f_C is defined as an indefinite integral (see appendix to Labrosse, 2015),

$$f_C(x, \delta) = 3 \int (1 - x^2 - A_\rho x^4)^{1+\delta} x^2 dx$$
$$= x^3 \left[1 - \frac{3}{5}(1+\delta)x^2 - \frac{3}{14}(1+\delta)(2A_\rho - \delta)x^4 + O(x^6) \right]. \tag{10}$$

Before the onset of IC crystallization, the central temperature T_0 evolves according to

$$Q_{CMB} - Q_R = - \int_{V_C} \rho_a C_p \frac{\partial T_a}{\partial t} dV = -\frac{4\pi}{3} \rho_0 C_p L_\rho^3 f_C \left(\frac{r_C}{L_\rho}, \gamma \right) \frac{dT_0}{dt}, \tag{11}$$

where $C_p = 750$ J/K/kg is the specific heat of iron at high pressure and temperature, and Q_R is the radiogenic power in the core,

$$Q_R = M_C h(t) = \frac{4\pi}{3} \rho_0 L_\rho^3 f_C \left(\frac{r_C}{L_\rho}, 0 \right) h(t). \tag{12}$$

We assume the amount of thorium and uranium to be negligible in the core (Chidester et al., 2017; Wipperfurth et al., 2018), making the decay of potassium the only possible significant radiogenic heat source. We choose the concentration of potassium in the core to be either 0 or 200 ppm, the latter is usually considered to be an upper limit (Hirose et al., 2013).

Once the inner core starts crystallizing, that is, once the central temperature T_0 reaches T_{L0}, its radius evolves as

$$r_{IC} = r_{IC_p} \left(\frac{t}{a_{IC}} + 1 \right)^{0.4}, \tag{13}$$

where $r_{IC_p} = 1221$ km is the present-day IC radius and a_{IC} is the age of the IC. The IC growth is governed by core energetics, which includes

latent heat of freezing, changes of compositional energy, secular cooling, and radioctive heating. Eq. (13) is an approximate relation that fits the numerical solution of this complex problem, under the assumption that the amount of total dissipation in the core is constant (Labrosse, 2015). Thanks to Eq. (13) we can avoid computing the energetics of IC growth here. The age of IC is then determined simply as

$$a_{\text{IC}} = (\mathscr{L} + \mathscr{X} + \mathscr{C}) \left[\frac{Q_{\text{CMB}}(r_{\text{IC}} = 0) + Q_{\text{CMB}}(r_{\text{IC}} = r_{\text{IC}_p})}{2} - Q_R(t = 0) \right]^{-1},$$

(14)

with the total latent heat released during the crystallization being $\mathscr{L} = 6.88 \times 10^{28}$ J, the total compositional energy released being $\mathscr{X} = 4.69 \times 10^{28}$ J, and the secular cooling contributing $\mathscr{C} = 18.13 \times 10^{28}$ J since the onset of freezing (Labrosse, 2015) (below we label the sum of these terms as E_{IC}). Eq. (14) assumes Q_{CMB} to vary linearly with time between the onset of IC and the present-day and is only zeroth-order accurate with respect to the time variation of Q_R. Since the contribution of Q_R is small, the resulting error is negligible.

The heat flow at the core-mantle boundary Q_{CMB} is governed by mantle convection. Indeed, with respect to the vigorously convecting liquid core, the mantle acts as a thermal insulator and thus determines the amount of heat extracted from the core. Here, however, we aim to obtain the minimum amount of heat that must be extracted from the core to sustain its dynamo, which, as is known from paleomagnetical record, has operated throughout most of its history (e.g. Aubert et al., 2009).

Following Labrosse (2015), we set Q_{CMB} to be slightly higher (by a factor $\theta \gtrsim 1$) than the conductive heat flow along the core's isentrope T_a near the CMB:

$$Q_{\text{CMB}} = \theta 4\pi r_{\text{C}}^2 k(r_{\text{C}}, T_{\text{CMB}}) \left(\frac{\partial T_a}{\partial r} \right)_{r=r_{\text{C}}},$$

(15)

where $T_{\text{CMB}} = T_a(r_{\text{C}}, r_{\text{IC}})$ and $k(r, T_{\text{CMB}})$ is the depth and temperature dependent thermal conductivity of iron, given by Gomi et al. (2013):

$$k(r, T_{\text{CMB}}) = k_{\text{CMB}_p} \left[1 + \frac{k_{6000} - 1}{6000 - T_{\text{CMB}_p}} (T_{\text{CMB}} - T_{\text{CMB}_p}) \right] \frac{1 - Y_k \left(\frac{r}{r_{\text{C}}} \right)^2}{1 - Y_k},$$

(16)

where $k_{\text{CMB}_p} = 90$ W/m/K, $k_{6000} = 1.52182$, $Y_k = 0.446989$, and $T_{\text{CMB}_p} = T_a(r_{\text{C}}, r_{\text{IC}_p})$ is the present-day CMB temperature. As discussed by Labrosse (2015), prior to the onset of IC crystallization the parameter θ must be greater than 1.14 in order to obtain a non-negative dissipation in the core as a whole (see Fig. 4 therein). As discussed later, after the onset of IC crystallization this condition is relaxed (Fig. 6 therein).

The temperature gradient in Eq. (15) can be directly computed from Eq. (8),

$$\left(\frac{\partial T_a}{\partial r} \right)_{r=r_{\text{C}}} = T_0 \gamma \left(1 - \frac{r_{\text{C}}^2}{L_\rho^2} - A_\rho \frac{r_{\text{C}}^4}{L_\rho^4} \right)^{\gamma-1} \left(-2\frac{r_{\text{C}}}{L_\rho^2} - 4A_\rho \frac{r_{\text{C}}^3}{L_\rho^4} \right).$$

(17)

Eqs. (11), (12), (15), and (17) can be combined into a single ordinary differential equation for T_0, which we integrate backward in time in order to obtain the core's thermal evolution prior to the onset of IC crystallization.

In Fig. 3 we plot the resulting evolution of $Q_{\text{CMB}}(t)$, the parameter θ being set to a time-independent value $\theta = 1.15$. We cannot reproduce the results of Labrosse (2015) using his reported parameter values. As illustrated by the red dashed line in Fig. 3, we can reproduce the solid black curves in his Figs. 11a and 13 when we use a different value of heat capacity, $C_p = 475$ J/K/kg. We discussed the mismatch with the author, who then found a numerical error in the algorithm that was used for computing the evolution of T_{CMB}, the effect being similar to employing an incorrect value of iron heat capacity (Stéphane Labrosse, personal communication). We note that our finding makes the model of

Labrosse (2015) even more plausible, as it leads to a reduction of the rather high values of T_{CMB} in the past, reducing the amount of predicted melting in the lower mantle.

The maximum age of the IC resulting from the model of Labrosse (2015) is ca. 600 Myr. The relatively young IC is in agreement with the most recent paleomagnetic findings (for a discussion, see Bono et al., 2019).

3.2. Results: Implications for the thermal history of the mantle

In the following we couple the evolution of $Q_{\text{CMB}}(t)$ computed in Section 3.1 with the parametrized model of mantle convection discussed in Section 2. Since the model of the core in Section 3.1 provides only the lower bound on Q_{CMB}, we can only aim at obtaining the upper bound on the possible amount of radiogenic heat in the mantle. For this reason, we mostly focus on simulations that assume potassium to have a concentration of 200 ppm in the core, and explore the results with [K] = 0 ppm on the side (the minimum heat flow from the core Q_{CMB} is smaller with the radiogenic heat than without – see the black vs. red line in Fig. 3).

When $Q_{\text{CMB}}(t)$ from Fig. 3 is used in Eq. (1), the resulting $H(t) + Q_{\text{CMB}}(t)$ curve is not very different from simply taking a $H(t)$ curve with a higher value of H_0. As a result, the qualitative behaviour of the numerical solution is similar to that discussed in Section 2.2; only the exact value of the transition solution H_0^* is different. In Fig. 4 we do the same as in Fig. 1, only this time Q_{CMB} is set to the minimum value required for the Earth's dynamo to operate (black curve on the left panel of Fig. 3). The transition solution shifts to $H_0^* \approx 16.0$ TW present-day (mantle) radiogenic power, corresponding to a Urey ratio of ≈ 0.43.

According to a recent summary by Jaupart et al. (2015), the geochemical inference on H_0 is in the range 9–17 TW. Therefore taking the minimum Q_{CMB} into account shifts H_0^* within the bounds of geochemical estimates.

In Fig. 5 we systematically vary the constant parameter θ, and for each value we plot the corresponding H_0^*. The transition values H_0^* are obtained by a similar procedure as in Figs. 1 and 4, with the transition criterion being $T_m(-4.5\,\text{Gyr}) = 1800$ K (i.e., $T_m(-4.5\,\text{Gyr}) > 1800$ K are considered as "hot" solutions and $T_m(-4.5\,\text{Gyr}) < 1800$ K as "cold" histories, but the exact choice of transition criterion makes little difference). We show the results for $\beta = 1/3$ and $\beta = 0.27$ (Fig. 5, the red circles and squares respectively). As expected, increasing θ leads to a reduction of H_0^*. Accounting for radioactive sources in the core affects H_0^* in the opposite direction, but the effect is marginal (red crosses in Fig. 5).

For the parameters from Labrosse (2015), the present-day temperature gradient along the core's isentrope is 0.97 K/km at $r = r_{\text{C}}$, making the present-day Q_{CMB} equal to 14.6 TW for $\theta = 1.15$ (Eq. (15)). When the values $Q_S^0 = 38$, $H_0 = 16.0$, and $Q_{\text{CMB}} = 14.6$ TW are inserted into Eq. (1), one obtains a present-day secular cooling of 32 K/Gyr. This is less than what the geological and petrological records suggest (e.g. Abbott et al., 1994; Nisbet et al., 1993; Herzberg et al., 2010). In Fig. 5, we mark the values of H_0 that yield present-day secular cooling in the range 50–100 K/Gyr in green (this region is obtained directly from Eq. (1) by setting $Q_S^0 = 38$ and $t = 0$, and with Q_{CMB} set according to Eq. (15) for the present-day isentrope inside the core).

Once the IC starts crystallizing, the amount of total dissipation rises rapidly in the core (see Fig. 11b of Labrosse (2015)). This means that after the onset of IC it becomes much easier to sustain the geodynamo – the present-day CMB heat flow could be much smaller than what was needed to operate the geodynamo prior to the onset of IC. Labrosse (2015) argues that since Q_{CMB} is governed by mantle convection and the dynamo has probably been operating continuously in the past, there is no reason why Q_{CMB} should suddenly drop at the time corresponding to the onset of IC. The condition for running a dynamo in an entirely liquid core is thus extended until present-day in his models.
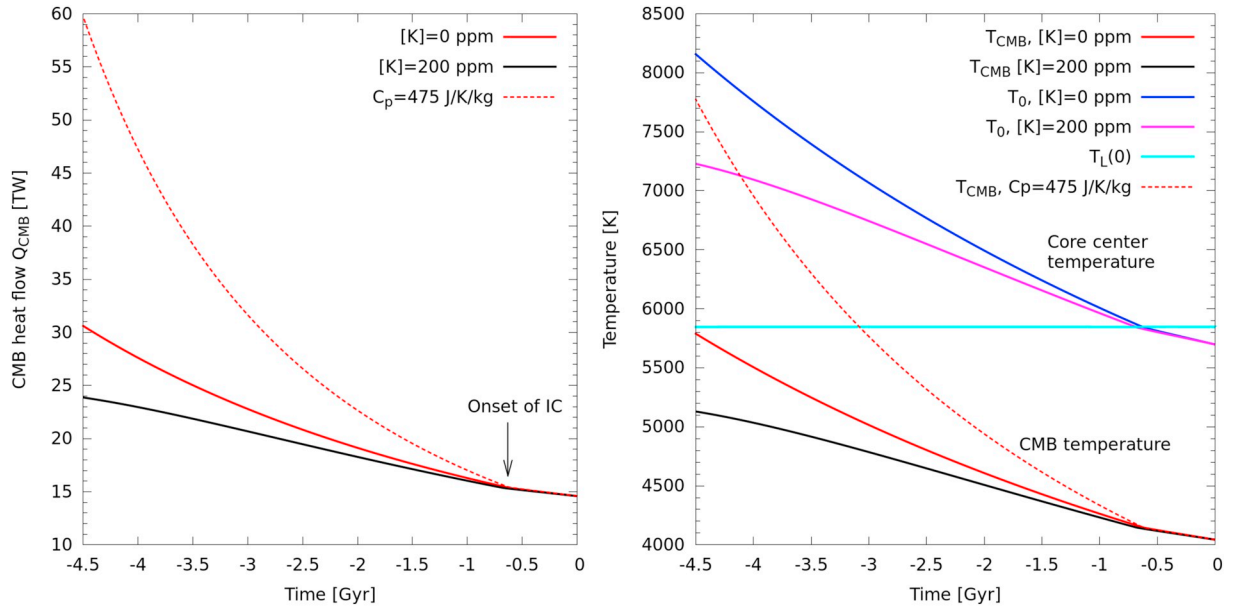
Fig. 3. (left) Evolution of the minimum heat flow out of the core Q_{CMB} required to sustain Earth's dynamo. The parameter θ is set equal to a time-independent value $\theta_0 = 1.15$, chosen to maintain the total dissipation in the core positive. We show both the situation without radiogenic heating in the core, [K] = 0 ppm, and the situation with 200 ppm of radiogenic potassium. (right) Evolution of the temperature at the core's center (T_0) and at the CMB (T_{CMB}). $T_L(0)$ is the central temperature at the onset of IC. The red dashed lines are nearly identical to the black solid lines in Figs. 11a and 13 of Labrosse (2015) and were obtained by setting $C_p = 475$ J/K/kg and [K] = 0 ppm (see text for discussion).

In the following we employ a different approach. The mantle was hotter in the past and convection was likely to be more vigorous. Under the assumption that Q_{CMB} was higher for the more vigorously convecting mantle, it is possible that the present-day Q_{CMB} is below the level that was necessary to maintain the dynamo action without latent heat and compositional convection (i.e. prior to the crystallization of the IC). In other words, it is possible that the present-day value of θ is smaller than 1.15. It is thus reasonable to explore models in which the parameter θ is set to a constant value $\theta_0 \geq 1.15$ prior to the onset of IC nucleation and then decreases linearly until some present-day value θ_p is reached:

$$\theta(t) = \theta_p - \left(\theta_0 - \theta_p\right)\frac{t}{a_{IC}}, \quad t > -a_{IC}. \tag{18}$$

The lower limit on θ_p is ≈ 0.55 because for $\theta_p < 0.55$ the present-

day CMB heat flow becomes less than 7 TW, which is the minimum value required for a non-negative dissipation in the present-day outer core (see Fig. 6a in Labrosse, 2015).

In Fig. 6 we systematically explore the range of admissible values of θ_0 and θ_p. When $\theta_p < \theta_0$, the slope of $Q_{CMB}(t)$ increases during IC growth (i.e. $|t| < a_{IC}$) and the transition solutions have larger secular cooling. For the values of θ_0 and θ_p depicted by solid squares in Fig. 6, the transition solution has the following properties: i) secular cooling matches the petrologically inferred boundaries, ii) the Urey ratio is in agreement with geochemical models of the Earth's composition ($9 < H_0^* < 17$ TW), and iii) the mantle potential temperature remains below 2000 K throughout Earth's history. In other words, the thermal catastrophe is avoided. The colour of the symbols on the left panel of Fig. 6 represents the transition value H_0^*. Note that the y-axis is cut-off at $\theta_p = 0.55$, which is the critical value that corresponds to $Q_{CMB}^0 = 7$ TW.
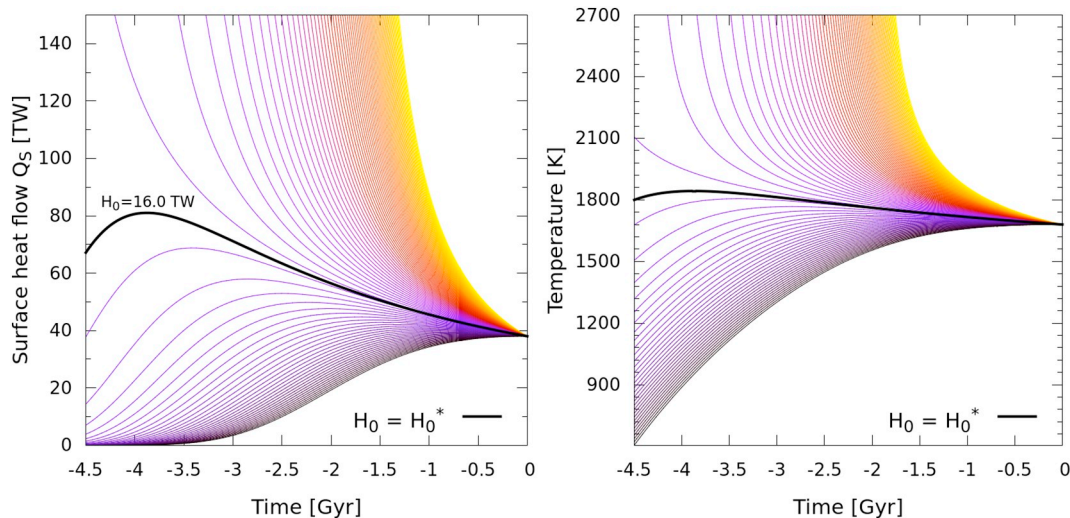

Fig. 4. (left) As Fig. 1, only here the heat flow from the core is not zero, but follows the black curve from Fig. 3. As a result, the transition value H_0^* shifts to 16.0 TW, making the present-day Urey ratio 0.43 (black line). (right) The mantle potential temperature of the respective simulations.
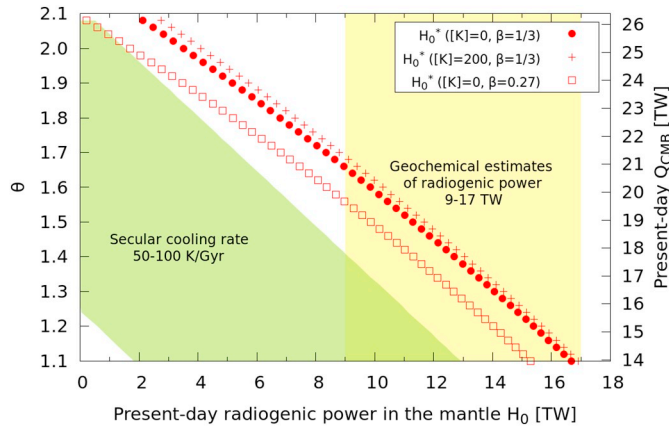
Fig. 5. Dependence of the transition value H_0^* on θ. The time-constant parameter θ is systematically varied from 1.1 to 2.1 and for each value we compute the amount of radiogenic heat H_0^* that marks the boundary between "hot" and "cold" histories, using the *Nu–Ra* scaling law with exponent $\beta = 1/3$ (red circles) or $\beta = 0.27$ (red squares). The light green region covers the values of H_0 that yield present-day secular cooling in the range 50–100 K/Gyr (obtained directly from Eq. (1), with $Q_S = 38$ TW and Q_{CMB} following Eq. (15) for the present-day core's isentrope). The right axis shows present-day Q_{CMB}^0 obtained for the corresponding value of θ. The 9–17 TW range inferred from geochemical BSE models is in yellow. (For interpretation of the references to colour in this figure legend, the reader is referred to the web version of this article.)

Allowing for radioactive sources in the core shifts the range of admissible θ_0 to slightly higher values, but its effect is rather small (right panel). The colour of the symbols on the right panel of Fig. 6 has a different meaning than on the left panel and is discussed below. Note that the range of θ_p for which the thermal catastrophe is avoided (i.e. the above conditions i–iii are satisfied) becomes broader if a smaller value of β is assumed, that is, when the surface heat flow is more weakly dependent on the mantle temperature T_m. Similar effect has lowering the activation energy E_{act}. Since $\beta = 1/3$ is rather the upper estimate of the respective quantity, the range of θ_0 and θ_p for which admissible solutions are obtained would be broader if the parameter was varied (or if E_{act} was lowered).

The above conditions i–iii are only the most basic observations that one can use for constraining thermal history models. Indeed, various
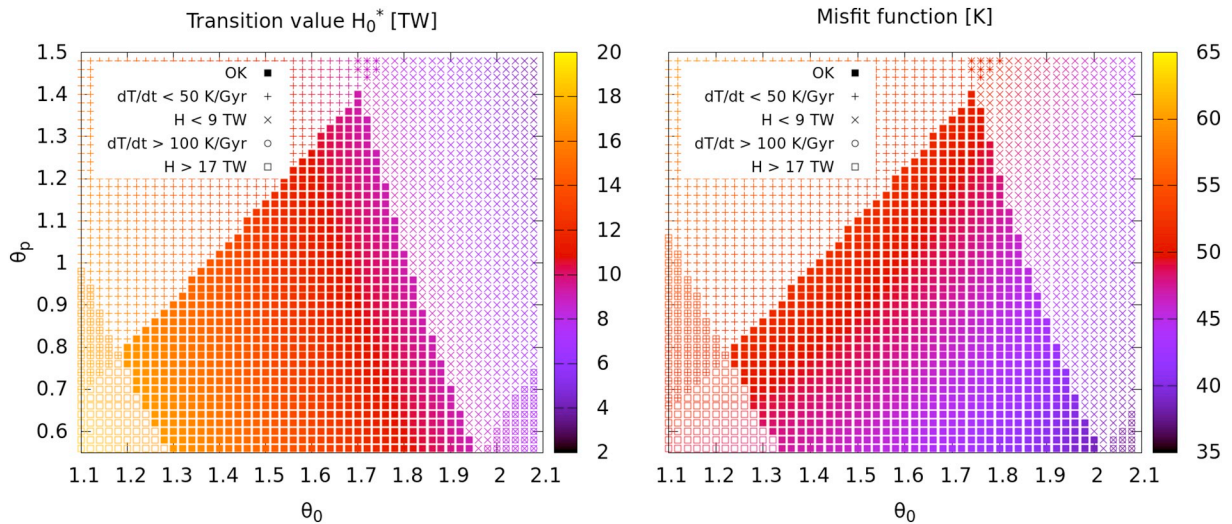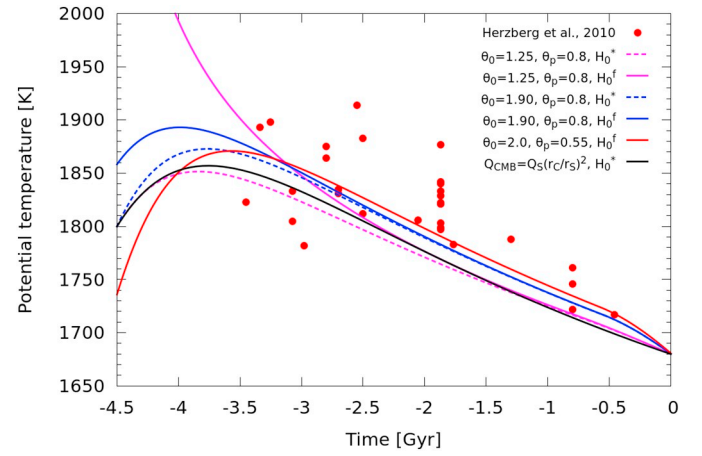

Fig. 7. Comparison of computed thermal histories with the petrological data collected by Herzberg et al. (2010) (red circles). The pink and blue dashed lines show transition solutions that are obtained by using $\theta_p = 0.8$ (fixing the present-day Q_{CMB} to ~10 TW) and $\theta_0 = 1.25$ and 1.90 respectively. The solid lines show solutions with the smallest possible misfit with respect to the data. For $\theta_0 = 1.90$ and $\theta_p = 0.8$, $H_0^* = 9.28$ TW and $H_0^f = 9.26$ TW (blue). For $\theta_0 = 1.25$ and $\theta_p = 0.8$, $H_0^* = 16.65$ TW and $H_0^f = 16.50$ TW (pink). For the red line, $H_0^f = 9.18$ TW and the misfit is the smallest (cf. Fig. 6). The amount of radioactive potassium in the core is [K] = 200 ppm for all the plotted solutions. (For interpretation of the references to colour in this figure legend, the reader is referred to the web version of this article.)

geological and petrological studies provide additional clues as to how the temperature of the Earth's mantle varied in the past and how hot the mantle was when it formed through crystallization of the primordial magma ocean.

In Fig. 7 we compare the thermal history of selected transition solutions with the data set of Herzberg et al. (2010), consisting of source temperatures inferred for non-arc Archean and Proterozoic basalts that can be used as a proxy for the evolution of the mantle potential temperature. For clarity of the figure, we show only two transition solutions. They both have θ_p equal to 0.8, corresponding to Q_{CMB}^0 of ~10 TW, and θ_0 is taken from the edges of admissible solutions depicted in Fig. 6, that is, 1.25 and 1.90 respectively. As discussed above, the slope of $T_m(t)$ during IC growth is governed by the difference $\theta_0 - \theta_p$ and is

Fig. 6. Systematic exploration of the θ_0, θ_p space. (left) The amount of radiogenic sources in the core is considered negligible, [K] = 0 ppm, and the points are colored according to the transition value H_0^* in TW. Transition solutions with $9 < H_0^* < 17$ TW and $50 < \frac{dT}{dt|_{t=0}} < 100$ K/Gyr are plotted as filled squares. (right) The concentration of radiogenic potassium is 200 ppm and the points are colored by the lowest misfit relative to the petrological data (i.e. by the value of $\sqrt{\sum_i^n (T_{dat}(t_i) - T_m^f(t_i))^2/n}$, where T_m^f corresponds to the solution obtained by setting $H_0 = H_0^f(\theta_0, \theta_p)$ – see also Fig. 7).

thus steeper when θ_0 is larger (see the difference between the secular cooling rate of the pink and blue dashed lines in the time window of 0 to -0.6 Gyr). Prior to the onset of IC crystallization, the slope of T_m is governed by θ_0 only and is thus also slightly steeper for the blue dashed line. The difference is, however, almost indistinguishable because the total heat source $H + Q_{CMB}$ is dominated by the internal heating H in both cases.

The transition solutions seem to provide a reasonable fit to the petrological data set. Nevertheless, it is also possible to search for a value of H_0 that results in a thermal history providing the best fit to the data. Solid lines in Fig. 7 correspond to such solutions, with the misfit being defined as the L2 norm of the difference between the computed $T_m(t)$ and the data, i.e. $\sqrt{\sum_i^n (T_{dat}(t_i) - T_m^f(t_i))^2/n}$. The best-fit values of H_0 are labeled as H_0^f. Due to reasons explained in Section 2.2, for given θ_0 and θ_p the best-fit value H_0^f differs from H_0^* by less than 1%.

The best-fit solutions may be both non-monotonic or monotonic and their initial temperature may be either higher of lower than 1800 K. On the right panel of Fig. 6, the points are colored according to the misfit of the best-fit solution for each θ_0 and θ_p. The lowest values of misfit are reached in the right bottom corner of the admissible ranges of θ (see also the red solid line in Fig. 7).

Note that all the best-fit and transition solutions studied in this section fit only the bottom edge of the observed mantle temperatures in the time window from -3 to -1 Gyr. To understand this, we must recall that, as discussed above, the IC is only ca. 600 Myr old in our models, and prior to the onset of IC the secular cooling of the mantle is governed by θ_0 only. Moreover, while decreasing θ_0 makes Q_{CMB} smaller and could thus result in faster secular cooling, this is not happening, because a smaller θ_0 also implies more radiogenic heating in the mantle and the smaller Q_{CMB} is compensated by this increase in H^* (Fig. 5).

Preceding the models in the next section, we also plot $T_m(t)$ resulting from a simple heuristic model in which Q_{CMB} is linked to Q_S. In this model, we assume the heat flux at the CMB to be the same as the one measured at Earth's surface, setting $Q_{CMB} = Q_S(r_C/r_S)^2$. $H_0^* = 17.8$ TW for this model and the corresponding transition solution is similar to the one for $\theta_0 = 1.25$ (the black vs. pink dashed line in Fig. 7).

It is worth noting that setting θ_p lower than 1 leads to a region with a negative convective heat flow in the upper part of the liquid outer core (see Fig. 8 in Labrosse, 2015). Arguments for partial thermal stratification of the outer core can be found in the literature (Garnero et al., 1993; Tanaka, 2007; Helffrich and Kaneshima, 2010), although

Irving et al. (2018) have recently argued that a stratified layer is not required to explain the seismic data. However, a negative convective heat flow in some layer of the core does not necessarily mean thermal stratification of such layer, because buoyant plumes coming from underlying regions with positive convective heat flow can disturb the potentially stratified layer, as discussed e.g. in Labrosse (2015).

4. Models with mutual core-mantle coupling

In the real Earth, the amount of heat extracted from the core is governed by the dynamics of the lower mantle, specifically by the properties of the bottom thermal boundary layer. In this section, following the treatment of Driscoll and Bercovici (2014) (and similarly to the treatment of the top thermal boundary layer in Eq. (3)), we assume the heat flow from the Earth's core to be:

$$Q_{CMB} = S_C k_{LM} \frac{\Delta T_{LM}}{\delta_{LM}}, \tag{19}$$

where S_C is the surface area of the outer core, $k_{LM} = 10$ W/m/K is the lower mantle thermal conductivity, and $\Delta T_{LM} = T_{CMB} - T_{LM}$ is the temperature jump across the thermal boundary layer. The lower mantle temperature T_{LM} is an extrapolation of the mantle potential temperature T_m along the mantle adiabat, $T_{LM} \approx \exp(-(r_{CMB} - r_S)\alpha g / c_p)T_m \approx 1.86 T_m$. The thickness of the lower mantle thermal boundary layer is determined from the boundary layer theory:

$$\delta_{LM} = \left(\frac{\kappa \nu_{LM}}{\alpha g_{LM} \Delta T_{LM}} Ra_c\right)^{1/3}, \tag{20}$$

where we employ the values of thermal diffusivity κ, thermal expansivity α, gravitational acceleration g_{LM}, and critical Rayleigh number Ra_c that are used in Driscoll and Bercovici (2014) ($\kappa = 10^{-6}$ m^2/s; $\alpha = 3 \times 10^{-5}$ K^{-1}; $g_{LM} = 10.5$ m/s^2; $Ra_c = 660$). The kinematic viscosity of the lower mantle is computed as $\nu_{LM} = f_\nu \nu$, with the viscosity factor f_ν being varied between 2 and 10. We use here the same range and notation as Driscoll and Bercovici (2014), motivated by inferences from glacial isostatic rebound (Paulson et al. (2005) and mineral physics (Yamazaki and Karato, 2001). Only now the viscosity law (5) needs to be anchored. We also adopt the same reference viscosity as Driscoll and Bercovici (2014), $\nu_0 = 7 \times 10^7$ m^2/s, yielding $\nu = 1.5 \times 10^{17}$ m^2/s for the present-day potential temperature of 1680 K.
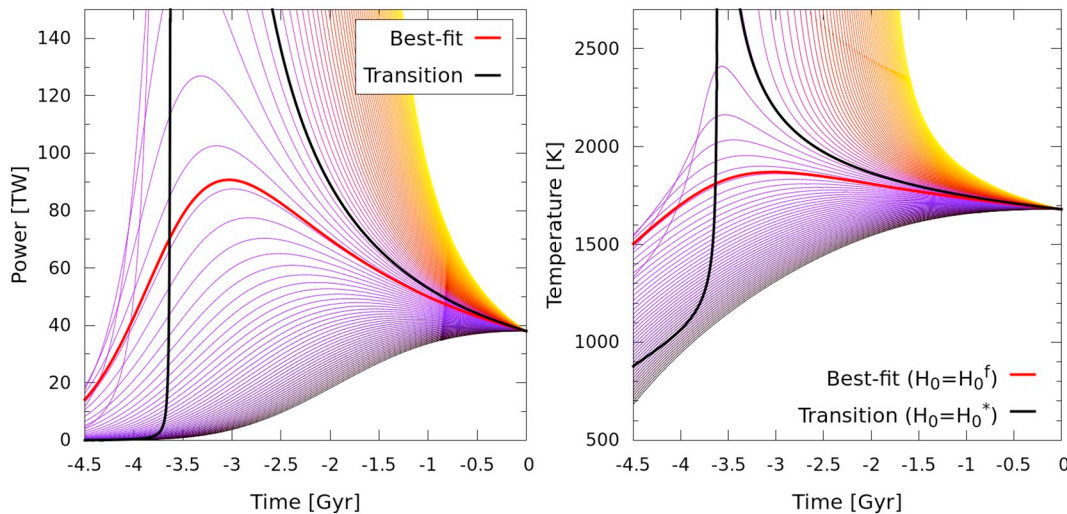

Fig. 8. Similar to Fig. 4. (left) The heat flow coming from the Earth's core follows Eq. (19). We show 100 backward-in-time solutions that differ in the value of H_0, evenly sampling the 0 to $(Q_S^0 - Q_{CMB}^0)$ range. The viscosity factor f_ν is equal to 5.0 and [K] = 200 ppm, making $Q_{CMB}^0 \approx 11.3$ TW. Transition (black) and best-fit (red) values deviate significantly for models with core-mantle feedback: $H_0^* = 14.71$ TW and $H_0^f = 16.25$ TW. (right) The mantle temperature T_m of the respective simulations. (For interpretation of the references to colour in this figure legend, the reader is referred to the web version of this article.)

Note that one still needs to compute the evolution of $T_{CMB}(t)$ in order to get the heat flow from Eq. (19), for which we employ the equations from Section 3.1. In particular, Eq. (11) is used to compute the Earth's center temperature prior to the onset of IC and Eqs. (8) and (13) are used to compute $T_{CMB}(t)$ during IC growth. To compute the age of IC in our backward integrations, we again employ Eq. (14). The only problem is that this time $Q_{CMB}(r_{IC}=0)$ is not known in advance of each simulation, because Q_{CMB} now depends on T_m. To overcome this obstacle, we make a first-order guess, $T_m(t=-a_{IC}) = T_m(t=0) - \frac{dT}{dt} \times a_{IC}$, which we solve iteratively with respect to a_{IC}. To determine the error introduced by using only a first-order estimate of $T_m(t=-a_{IC})$, we compute the time integral of $Q_{CMB} + Q_R$ over a_{IC} after each simulation and compare it with the energy of the IC growth $E_{IC} = \mathcal{L} + \mathcal{X} + \mathcal{C}$. The error never exceeds 3% (i.e. the IC has approximately the correct size in all our simulations).

In Fig. 8, similarly as in Figs. 1 and 4, we show a set of backward in time solutions obtained by evenly sampling H_0 from 0 to $Q_S^0 - Q_{CMB}^0$, with Q_{CMB} now following the $Q_{CMB}(T_m)$ relationship (19). The viscosity factor f_ν is set here to 5.0 and [K] = 200 ppm. The transition solution is marked by the thick black line and the best-fit solution is plotted in red, the respective values of present-day internal heating are $H_0^* = 14.71$ TW and $H_0^f = 16.25$ TW (these values are ca. 1 TW lower for [K] = 0 ppm, see Fig. 9).

Using Eq. (19) instead of (15) changes the mathematical nature of the governing equations, as the two ODEs for T_m and T_{CMB} are now coupled. The heat input $Q_{CMB}(t)$ is no longer known a priori and can take both very high and very low values. As explained in Appendix A, the key parameter controlling the core-mantle feedback is the viscosity factor f_ν. For $f_\nu \lesssim 8$, the best-fit value H_0^f no longer follows the transition value H_0^* closely, and it is no longer true that for any reasonable $T_m(t=-4.5\,\text{Gyr})$ the forward integration would converge towards the transition solution. Instead of H_0^*, we thus pay closer attention to H_0^f in the following - its vicinity represents the physically acceptable solutions better in this class of models (see Appendix A for detailed justification).

For models with core-mantle feedback, we show in Fig. 9 the dependence of H_0^f on f_ν, in analogy to Fig. 5. We see that the higher the viscosity contrast f_ν, the more radiogenic heating in the mantle is predicted by these models. For the traditional scaling $\beta = 1/3$, there is a range of f_ν spanning roughly from 2.5 to 6, for which the solutions satisfy the observational constraints i) $9 < H_0^f < 17$ TW, and ii)
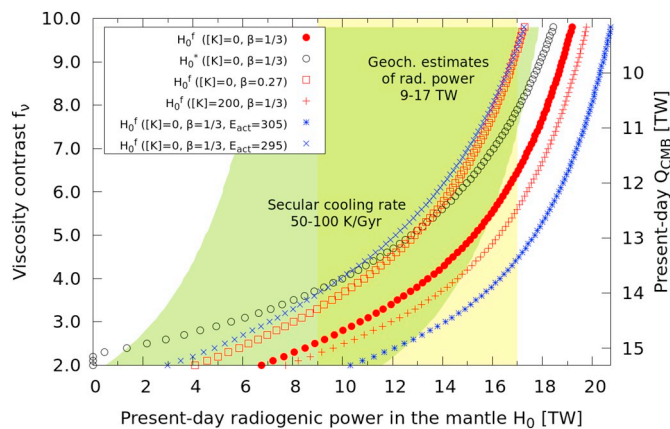

Fig. 9. Similar as Fig. 5, only for the models with core-mantle feedback. The varied parameter is the viscosity contrast between the lower and the upper mantle, f_ν. We show the dependence of the transition value H_0^* (black circles), as well as the best-fit value H_0^f (red circles) on f_ν. Only a limited range of viscosity contrasts yields solutions with $9 < H_0^f < 17$ TW and with present-day secular cooling being less than 100 and more than 50 K/Gyr. For *Nu–Ra* scaling with a milder temperature dependence this range is larger (red squares). The results are extremely sensitive to the exact value of E_{act} (blue crosses). (For interpretation of the references to colour in this figure legend, the reader is referred to the web version of this article.)
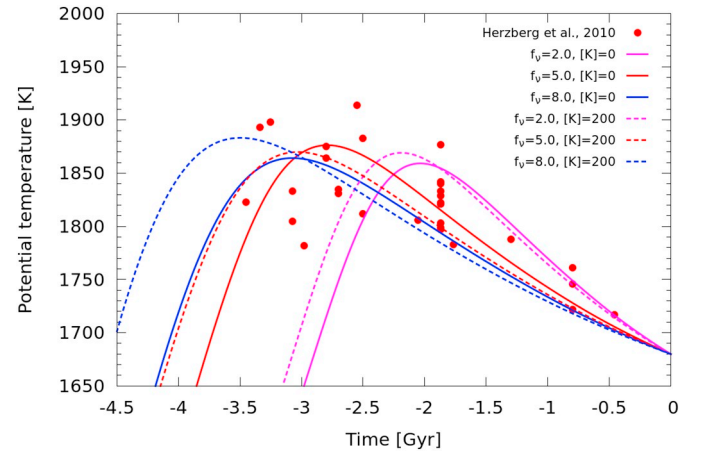

Fig. 10. As Fig. 7, only here we show the best-fit solutions for models with Q_{CMB} being linked to the mantle temperature T_m. For small values of the viscosity factor f_ν, the solution reaches maximum relatively early in Earth's history and drops sharply as one proceeds with integration further towards $t \to -4.5$ Gyr (dashed and solid pink lines). All the best-fit solutions are non-monotonic for this type of models. (For interpretation of the references to colour in this figure legend, the reader is referred to the web version of this article.)

$50 < dT/dt(t=0) < 100$ K/Gyr. The maximum admissible value of the viscosity factor increases to nearly 10 if the condition $\beta = 1/3$ is relaxed by assuming a smaller value of 0.27 (the red squares in Fig. 9). Similarly as in Fig. 5, including radioactive sources in the core shifts the best-fit value H_0^f to higher values and leads to a decrease in the present-day secular cooling (for a given f_ν). Note that H_0^* and H_0^f become closer as f_ν is increased, which is explained in Appendix A.

In Fig. 10 we show selected thermal evolutions and compare them with the petrological record. By solid red line we mark the best-fit solution obtained with $f_\nu = 5$, for which $H_0^f = 15.2$ TW and K/Gyr. In pink and blue we plot the best-fit solutions for $f_\nu = 2$ and 8, for which $H_0^f = 6.8$ and 18.2 TW, respectively (i.e. outside the ⟨9,17⟩ TW range).

Note that all the best-fit solutions are non-monotonic. Maxima of the curves are attained at times ranging from -2 to -4 Gyr, depending on the value of the viscosity contrast between the lower and upper mantle f_ν. Increasing f_ν pushes the extreme further in history.

In view of reconciling Earth's thermal evolution, it seems troubling that T_m decreases relatively sharply as $t \to -4.5$ Gyr, reaching rather small values at the time of Earth's formation, especially for the $f_\nu = 2$ case. As explained in Appendix A, this is not due to the lack of the fitted data in the Hadean – it is rather an intrinsic property of models with core-mantle coupling. Three mechanisms help in increasing the obtained mantle initial temperature: i) increasing f_ν, ii) assuming a larger energy of IC growth, or iii) including more radioactive sources in the core (Figs. A3 and 11).

The difficulty in fitting the petrological record with $f_\nu < 4$ is also apparent when computing a misfit function quantifying the fit to the petrological data (Fig. 11). As analyzed in detail in Appendix A, the range of $T_m(-4.5\,\text{Gyr})$ that one obtains in backward in time simulations by varying H_0 from 0 to $Q_S^0 - Q_{CMB}^0$ is limited in models with $Q_{CMB} = Q_{CMB}(T_m)$ (in the models of Section 3.2 this was not a problem). The right axis of Fig. 11 shows the upper bound of $T_m(-4.5\,\text{Gyr})$ that can be reached for a given value of f_ν (cf. also Fig. A3, the plotted values in Fig. 11 correspond to the peak values of curves on the left panel of Fig. A3). Since the maximum value of $T_m(-4.5\,\text{Gyr})$ is always reached for H_0 that is in the vicinity of H_0^f, the dashed lines in Fig. 11 can be interpreted simply as $T_m(-4.5\,\text{Gyr})$ of the best fit solution – see also Figs. 8 and A5. Since the Earth formed hot and its global magma ocean solidified when its potential temperature cooled down to ca. 1800 K (Litasov and Ohtani, 2002, e.g.), having $T_m(-4.5\,\text{Gyr}) \geq 1800$ K may serve as yet another constraint that successful thermal histories must
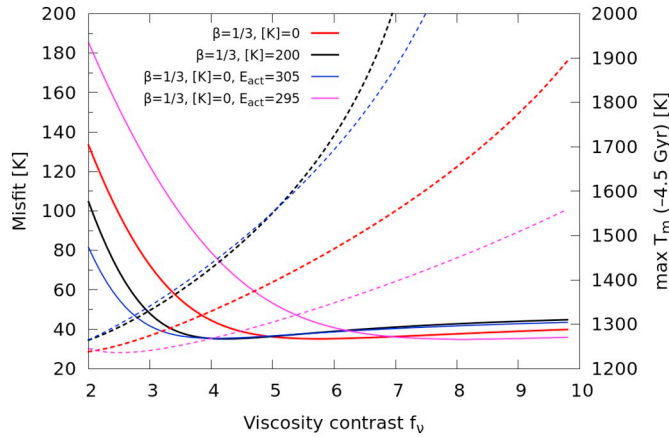
Fig. 11. Misfit of the best-fit solutions depicted in Fig. 10 as a function of the viscosity contrast f_ν. Dashed lines correspond to the maximum value of T_m (-4.5 Gyr) for a given f_ν (right axis). Colour of the dashed lines matches the labels for the solid lines.

obey.

Increasing f_ν expands the range of $T_m(-4.5$ Gyr), which explains the sharp decrease of misfit for $f_\nu > 4$ (solid red line in Fig. 11). Note that the initial mantle temperature is quite sensitive also to the amount of radioactive potassium in the core. While f_ν must be greater than 9 for reaching a mantle potential temperature of around 1800 K at time $t = -4.5$ Gyr, the same is possible for $f_\nu = 6$ with [K] = 200 ppm, and also the misfit function becomes flat already for $f_\nu > 3$ (dashed and solid black lines in Fig. 11). This may explain why Driscoll and Bercovici (2014) required radioactive sources in the core to obtain plausible models.

Finally, in Fig. 12 we compare the evolution of Q_{CMB} for selected best-fit models from this and the previous sections. For $f_\nu \leq 5$ the coupled models satisfy the dynamo constraint throughout Earth's history, while for $f_\nu > 5$ the heat flow from the core is less than 1.15 times the heat conducted along the core's isentrope. This constraint limits the admissible range of f_ν in the opposite direction than the $T_m(-4.5$ Gyr$) \approx 1800$ K constraint. The time period for which models with $f_\nu > 5$ fail to operate the dynamo is, however, a rather short window near $t = -a_{IC}$, and for f_ν as high as 10 the missing heat flow is

less than 20% of the required amount.

One could object that, since the minimum heat flow Q_{CMB} in Eq. (15) depends on the core temperature T_{CMB}, a direct comparison of $Q_{CMB}(t)$ curves from this and the previous sections is not entirely self-consistent. Indeed, Eq. (15) should be used together with $T_{CMB}(t)$ from each respective coupled model in order to check the dynamo constraint. However, using Eq. (15) together with the various red lines instead of the solid black line from the right panel of Fig. 12 does not change the above conclusions – the minimum heat flow required to operate the dynamo is nearly unaltered down to the Archean and is represented well by the minimum $Q_{CMB}(t)$ from Section 3.2.

Combining all the above mentioned observational constraints significantly limits the range of model parameters that yield satisfactory thermal histories. Nevertheless, for $f_\nu \approx 5$ and the traditional scaling with $\beta = 1/3$, our parametrized model matches the mantle source temperatures inferred for non-arc Archean and Proterozoic basalts, predicts H_0 within the geochemical BSE estimate of $\langle 9, 17 \rangle$ TW, yields present-day secular cooling of the mantle in the $\langle 50, 100 \rangle$ K/Gyr range, and extracts sufficient amount of heat from the core to continuously operate the geodynamo. The only issue, especially for [K] = 0 ppm, is that the initial temperature $T_m(-4.5$ Gyr$)$ is significantly below 1800 K. However, tectonics during the Hadean may have been very different from modern style plate tectonics (e.g., O'Neill and Debaille, 2014, see also Discussion]. As a consequence, the use of a simple scaling may not be able to capture the actual way in which mantle convection controlled the cooling of the interior. Because our best-fit models have a sharp decrease of temperature as $t \to -4.5$ Gyr, omitting the initial window of a few hundred Myr helps to overcome this last obstacle – already at $t = -4.2$ Gyr the above described solutions are well above 1700 K (cf. Fig. 8).

The initial CMB temperature stays below 8500 K for all our best-fit simulations (red lines on the right panel of Fig. 12) and for $f_\nu \geq 5$ it stays even below 6500 K. Such temperatures, however, still indicate widespread melting in the lower mantle and would result in a basal magma ocean, a plausible scenario (Labrosse et al., 2007), with potentially important implications for heat transfer in the lower mantle that have only started to be investigated (Agrusta et al., 2019). Under such conditions, Eq. (20) no longer holds. However, we perform backward-in-time simulations and our main constraints are petrological data that go back to 3.5 Gyr ago. Therefore, most of our conclusions
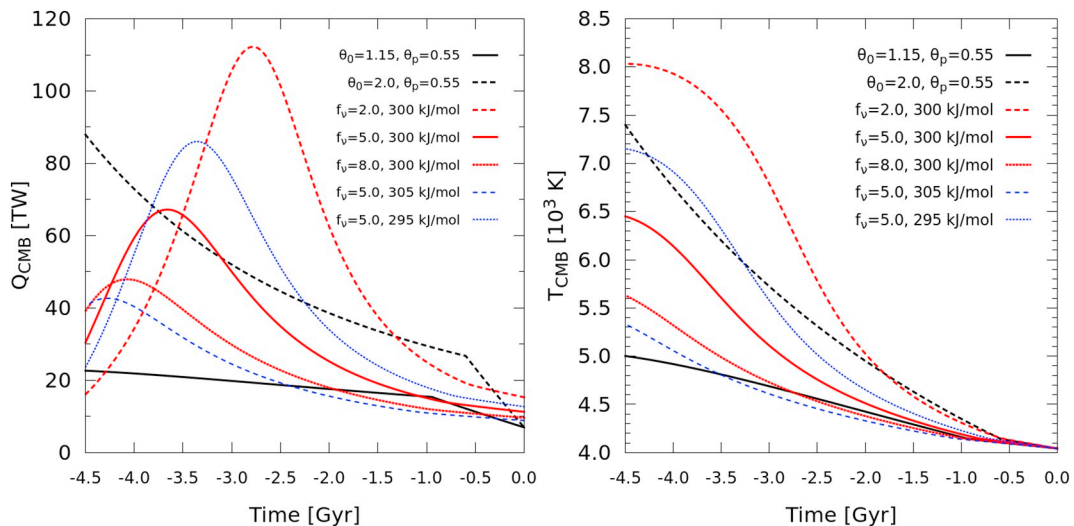

Fig. 12. (left) Evolution of Q_{CMB} for selected models from Sections 3.2 (black lines) and 4 (red and blue, $H_0 = H_0^f$ for these solutions). For a viscosity contrast between the lower and upper mantle smaller than 5, models with core-mantle feedback have sufficient heat-loss to drive the geodynamo (solid red vs. solid black line). Blue lines correspond to $f_\nu = 5$ and increased (dashed), resp. decreased (dotted) activation energy E_{act}. The concentration of radiogenic potassium in the core is 200 ppm for all the depicted solutions. (right) Evolution of T_{CMB} for the respective cases. (For interpretation of the references to colour in this figure legend, the reader is referred to the web version of this article.)

remain unchanged even though the early evolution is not accurately captured by the scaling laws that we use.

Note also that in the forward in time simulations of (Butler and Peltier (2002), for $T_m(-4.5 \, \text{Gyr}) = 8500 \, \text{K}$ their resulting Q_S^0 was still too low. Unlike in the present study, Butler and Peltier (2002) required unrealistically large $T_{CMB}(-4.5 \, \text{Gyr})$ in their whole mantle convection models in order to match the present-day heat flow, which led them to argue for a change in the degree of mantle layering in the past.

So far we have avoided discussing the role of the activation energy E_{act} in Eq. (5). As shown already in Fig. 9, our results are extremely sensitive to the value of E_{act} – using only 5 kJ/mol more (resp. less) than the reference 300 kJ/mol significantly shifts the best-fit $H_0 = H_0^f(f_\nu)$ curve down (resp. up). This sensitivity is a characteristic feature of the $Q_{CMB} = Q_{CMB}(T_m)$ models, while changing E_{act} by 5 kJ/mol has negligible effect when core-mantle coupling is not considered (Section 3.2). Consequently, any quantitative conclusions about the viscosity contrast f_ν must be treated with care, as they are intrinsically linked to the exact value of E_{act}.

While having a dramatic influence on our results, altering E_{act} does not help satisfy the observational constraints. This is because there is a direct trade-off between the activation energy and the viscosity contrast f_ν. As such, while slightly increasing E_{act} helps expanding the max $(T_m|_{t=-4.5})$ range, it simultaneously lowers the computed $Q_{CMB}(t)$, making it more difficult to comply with the dynamo constraint (cf. Figs. 11 and 12). The same mechanism applies when f_ν is increased. In fact, increasing E_{act} by 5 kJ/mol is similar to increasing the viscosity contrast f_ν by 2 (Figs. 9 and 11), and in terms of $Q_{CMB}(t)$ this trade-off is even stronger (Fig. 12).

The obtained evolution of Q_S and Q_{CMB} is non-monotonic for the models studied in this section: starting from $t = -4.5 \, \text{Gyr}$, the Earth's mantle first heats up, quickly reducing δ_{LM} (to about 50 km) and Q_{CMB} as well as Q_S are rising (Fig. 13). While the temperature difference ΔT_{LM} is steadily decreasing, $\delta_{LM}(t)$ reaches a minimum and $Q_{CMB}(t)$ reaches its peak in effect (cf. Eq. (19)). If the heat flow Q_{CMB} was monotonically decreasing instead, the resulting best-fit models would have much higher $T_{CMB}(-4.5 \, \text{Gyr})$.

Once both $H(t)$ and $Q_{CMB}(t)$ are decreasing, soon a balance between the heat sources and heat loss is obtained, i.e. $Q_S = Q_{CMB} + H$, after which the heat loss prevails and the mantle begins to gradually cool down until the present-day (Fig. 13). At the time corresponding to the maximum of $Q_S(t)$, the heat sources $Q_{CMB} + H$ are decreasing steeply
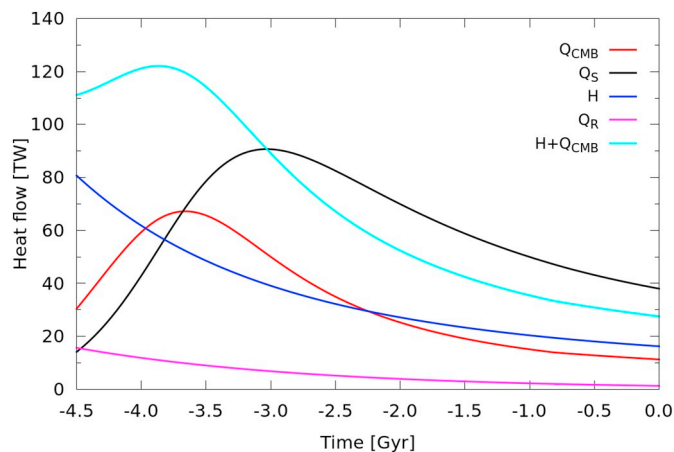

Fig. 13. Evolution of heat flows associated with the best-fit solution depicted in Fig. 8, that is for $f_\nu = 5.0$ and [K] = 200 ppm. The heat flow from the core Q_{CMB} is equally important as the radiogenic heating in the mantle H. When $Q_{CMB} + H$ match the heat loss from Earth's surface Q_S, the mantle temperature reaches its maximum (intersection of the light blue and black curves). (For interpretation of the references to colour in this figure legend, the reader is referred to the web version of this article.)

while Q_S is flat. Thanks to this effect, the secular cooling of the mantle quickly grows to well above 50 K/Gyr, resulting in a good fit with the mantle source temperature data in the time window of $t > -2$ Gyr (at least for $f_\nu \leq 5$, see Fig. 10).

Note that our $Q_{CMB}(t)$ is well above the lower bound of ca. 2 TW inferred from mantle plume activity by Sleep (1990) and also significantly larger than the heat flow resulting from the considerations of the minimum ohmic dissipation by Buffett (2002), consistently with our much shorter estimate of the age of the IC. It also roughly compares to $Q_{CMB}(t)$ resulting from the thermo-chemical mantle convection simulations of Nakagawa and Tackley (2013).

5. Discussion

The results presented in this paper are based on several underlying assumptions. First, the use of Eq. (2) implies that the radioactive elements do not escape the convecting mantle, an effect that has been considered in the context of mantle depletion and enrichment of the continental crust (e.g. Grigné and Labrosse, 2001; Cooper et al., 2006; Labrosse and Jaupart, 2007). It is equivalent to assuming that all the Earth's (continental) crust formed very early in Earth's history, a scenario favored by some authors (e.g. Armstrong, 1991; Rosas and Korenaga, 2018), but disputed by others (e.g. Belousova et al., 2010; Dhuime et al., 2012). Considering gradual instead of abrupt crustal growth would lower the computed values of H_0^* and H_0^f. Gradually adding more heat sources to the convecting mantle as one integrates backward in time means that the present-day value H_0 can be smaller while still avoiding the thermal runaway.

The presence of continents and other complexities of Earth-like plate-tectonics are implicitly accounted for in our governing equations, because the present-day estimates of T_0 and Q_S^0 are taken as input in Eq. (6). In other words, the reference point of the scaling is given by observations, and these of course include all the complexities of the Earth system.

However, the number of continents and their size have varied throughout Earth's history, and the effect of such variation is not well understood (Coltice et al., 2012). Our results are based on the assumption that the conventional $Nu \propto Ra^\beta$ scaling has always applied. Such assumption is indeed questionable, and should be tackled with the help of numerical models that account for intricacies of Earth-like mantle convection (i.e. including phase transitions, 3–D spherical geometry, plate-like tectonics, viscoelasticity, etc.). Recent results suggest that the role of melt generation and eruption should also be considered (Lourenco et al., 2018).

In the framework of parametrized convection, the role of melting was analyzed by Driscoll and Bercovici (2014), who showed its importance especially for stagnant lid planets and demonstrated that it may play a significant role in the early Earth. Our results are consistent with those of Driscoll and Bercovici (2014). We complement them by analyzing in detail the mutual relationship between $Q_{CMB}(t)$ and the mantle temperature. While Driscoll and Bercovici (2014) use only the present-day mantle temperature and convective heat flow to constrain their models, we include also petrological data. In particular, we analyze how the viscosity contrast between the lower and upper mantle influences the shape of the mantle temperature history $T_m(t)$, position of its maximum, and the capabilities of our models to recover initial mantle temperatures that correspond to the rheological transition of a global magma ocean.

Analyzing the mutual feedbacks between model parameters and finding successful models that simultaneously satisfy all the constraints required running tens of thousands of backward in time simulations – a task not possible with direct modelling of mantle flow. It is important to stress that our findings do not aim at replacing complex geodynamical models, but rather provide a guide on how to set-up 3–D numerical experiments that could self-consistently explain the Earth's thermal evolution.

An important drawback of the thermal evolutions resulting from models with core-mantle coupling is a sharp decrease of temperature in the Hadean Eon, making it difficult to reach initial temperatures consistent with models of the Earth's mantle formation. While we discuss some mechanisms that can resolve this issue, a likely scenario is also that convection in the Hadean mantle no longer matched our assumptions, e.g. due to a change in mantle layering as hypothesized by Butler and Peltier (2002), or that melting in the early Earth would serve as a thermostat (e.g. Armann and Tackley, 2012). Another possibility is that early Earth's mantle was predominantly in the mode of sluggish lid rather than active lid convection (Crowley and O'Connell, 2012)].

The idea that the dynamics of boundary layer at the bottom of the mantle is controlled solely by its stability is certainly simplistic, as it is likely influenced by additional factors such as variations of composition, phase transitions, and internal heating. For example, Nakagawa and Tackley (2005) show that the heat flow from the core may be significantly affected by the blanketing effect of subducted oceanic crust. Replacing Eq. (20) with a more realistic scaling, however, is yet to be done.

Assuming Eq. (20) holds, it still contains several unconstrained parameters, in particular Ra_c. We adopt, in accordance with Driscoll and Bercovici (2014), the critical value for the stability of the whole layer. As discussed in Sotin and Labrosse (1999), such approach is problematic. To this end, we note that the value of Ra_c, the thermal expansivity of the lower mantle, and also the viscosity pre-factor enter our calculations only through Eq. (20), where they appear together with the varied parameter f_ν. In other words, using e.g. a twice smaller value of Ra_c is identical to using a double viscosity contrast f_ν. Our results would thus remain unaltered, with the exception that the preferred lower/upper mantle viscosity contrast would shift to 10 instead of 5 (the same applies for α and ν_0).

As an alternative to the conventional models, O'Rourke et al. (2017) presented a parameterized thermal evolution model for the mantle coupled to the core, where they assume precipitation of Mg-bearing minerals in the core as the dominant mechanism for powering the geodynamo (O'Rourke and Stevenson, 2016). Hirose et al. (2017) argue that crystallization of silicon dioxide could have a similar effect. Such core dynamics would relax the requirement on high heat flow out of the core, but does not preclude it. Moreover, new experiments suggest that magnesium does not dominate the dissipation budget for the core, although it could still reduce the minimum Q_{CMB} by ca. 25% (Badro et al., 2018; Du et al., 2019).

In this paper we consider the radiogenic power in the mantle to be consistent with geochemical estimates when it fits within the range of 9 to 17 TW. In fact, it may be experimental neutrino physics which will soon guide the debate. Measurements of geoneutrinos emitted in decays of natural radionuclides in the crust and in the mantle have begun to place limits on Earth's radioactivity (Gando et al., 2013; Agostini et al., 2015). With the construction of three more experiments under way, collaboration between neutrino physics and geoscience must answer the challenge to place much tighter limits on the radiogenic heat content of the mantle. If the upper bound of 17 TW is to be lowered by geoneutrino measurements in the future, then our models would indicate either lower viscosity contrast between the lower and upper mantle, or lower value of the exponent β (Fig. 9). In view of Fig. 11, this would also indicate that in the early Earth the assumption of $Nu \propto Ra^\beta$ must have been violated.

6. Conclusions

We revisited conventional parametrized convection models of Earth's thermal history. By including recent estimates of the minimum amount of heat that must be extracted from the Earth's core in order to sustain the geodynamo, we show that the power of radiogenic heat sources in the mantle that is necessary to avoid the so-called thermal catastrophe (≈ 16 TW, Fig. 4) falls within the 9 to 17 TW range inferred from geochemical BSE estimates. As an additional constraint, we

compare the mantle temperature obtained from the parametrized models with the petrological record. If the condition for operating the geodynamo in an entirely liquid core is assumed to hold throughout the Earth's history (i.e. if heat from the core is assumed to exceed the heat conducted along the core's isentrope by a constant factor), our models predict secular cooling smaller than that observed in the petrological record. If, once the IC starts crystallizing, heat from the core is allowed to decrease more rapidly than the heat conducted along the core's isentrope, e.g. due to a decreasing vigour of mantle convection, then present-day secular cooling predicted by our parametrized model falls within the observed 50–100 K/Gyr range.

In the second part of this paper we turn to models in which the core-mantle heat flow is controlled by the insulating properties of the lower mantle. We show that, if the lower mantle is sufficiently more viscous than the upper mantle, the computed Earth's thermal histories fit well with the petrological record, reach their peak values in the Archean, are consistent with the mantle having an initial temperature of around 1800 K and the outer core being cooler than 7000 K, and indicate the amount of radiogenic heating in the mantle to be within the geochemical BSE estimate (on its upper edge). The CMB heat flow from these coupled models is consistent with operating the geodynamo throughout most of Earth's history, but to satisfy the dynamo constraint continuously throughout the age of the Earth, the viscosity contrast cannot be too high. For small viscosity contrasts, on the other hand, the fit to the petrological data is poor and the resulting solutions have unrealistically low initial mantle temperature. These shortcomings of models with small viscosity contrasts are partially eliminated when radiogenic potassium is included in the core. The range of successful model parameters, although being narrow, is not empty. This suggests that the classical $Nu \propto Ra^{1/3}$ scaling cannot be rejected on the grounds of yielding implausible Earth's thermal history.

The actual value of the lower-to-upper mantle viscosity contrast for which our parametrized model provides the best fit to the observational constraints is strongly sensitive with respect to the activation energy that governs the temperature dependence of mantle viscosity. There is a trade-off between these two parameters: using a higher activation energy shows a similar effect to using a larger viscosity contrast and vice versa. For activation energy of 300 kJ/mol, our preferred lower-to-upper mantle viscosity contrast is 5.

CRediT authorship contribution statement

V. Patoč**ka:**Conceptualization, Formal analysis, Investigation, Methodology, Software, Visualization, Writing - original draft.**O. Šrámek:**Conceptualization, Methodology, Funding acquisition, Supervision, Writing - review & editing.**N. Tosi:**Conceptualization, Methodology, Funding acquisition, Supervision, Resources, Writing - review & editing.

Declaration of competing interest

The authors declare that they have no known competing financial interests or personal relationships that could have appeared to influence the work reported in this paper.

Appendix A. Transition solution of models with core-mantle feedback

From Fig. 8 it is clear that the solution of Eqs. (1)–(6) behaves differently in models in which the heat flow from the core is coupled to the mantle temperature when compared to the behaviour described in Sections 2.2 and 3.2, where Q_{CMB} followed a predefined evolution. In this appendix, we describe the behaviour of the coupled models in detail.

When introducing the concept of a transition solution (resp. transition value H_0^*) in the main text, a key feature was that in the vicinity of H_0^* a small change of H_0 resulted in a large change of the mantle temperature at time $t = -4.5$ Gyr (producing either hot or cold histories of the Earth). For the coupled models, this feature becomes even more pronounced. As shown on the left panel of Fig. A1, the smallest numerically tractable difference in H_0 results either in the thermal catastrophe or in a mantle that is extremely hot near $t = -3.61$ Gyr, but cools sharply around $t = -3.62$ Gyr to less than 1000 K.

The right panel of Fig. A1 explains the underlying mechanism in terms of heat flows. As discussed above, Eq. (1) is a highly non-linear ODE with a tendency to result in the thermal runaway if the heat sources are insufficient. In the coupled models, however, the heat source Q_{CMB} is also governed by a non-linear ODE, and if $\delta_{LM} \to 0$ its solution also has a tendency to blow-up. This indeed does happen for a rapidly increasing mantle temperature (due to the dependence of δ_{LM} on both ν_{LM} and ΔT_{LM} – see Eq. (20)). If the growth of Q_{CMB} is rapid enough, it can reverse the evolution of the mantle temperature.

For the transition solution, both ΔT_{LM} and T_{LM} are increasing near $t = -3.61$ Gyr and the heat flow from the core rises sharply, eventually exceeding Q_S near $t = -3.62$ Gyr and moderating the mantle temperature in effect. For any $H_0 < H_0^*$, the temperature difference ΔT_{LM} starts decreasing instead and the mantle heats up beyond limits (numerically, we stop the simulation when $T_{CMB} = T_{LM}$, because otherwise we would have to complement Eqs. (19) and (20) with an additional rule for $\Delta T_{LM} < 0$).
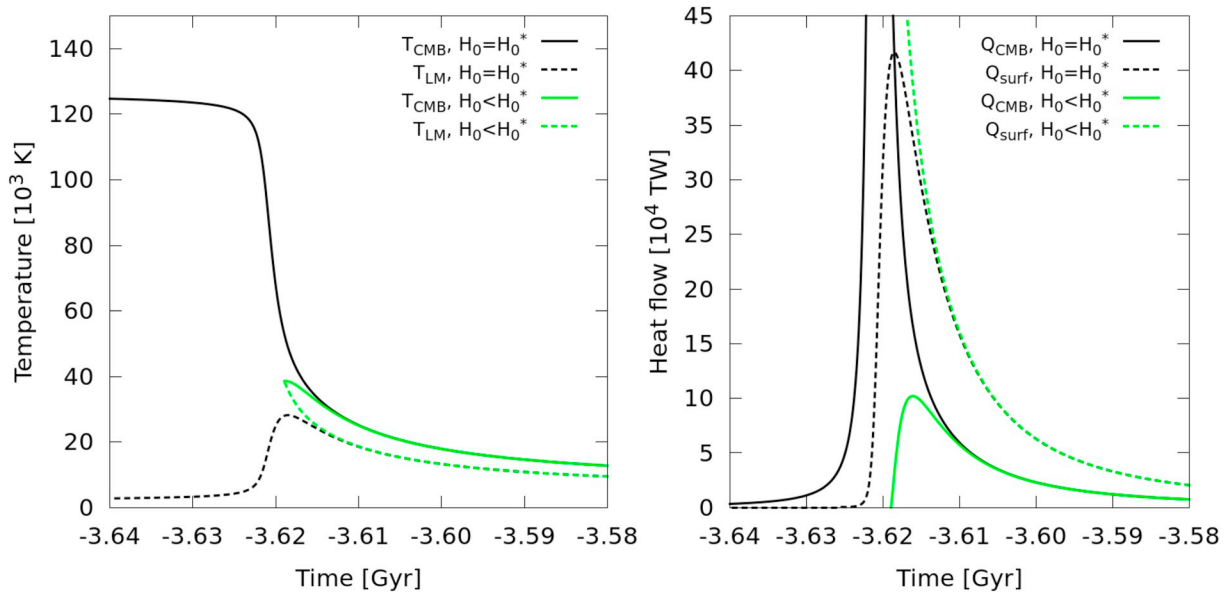

Fig. A1. Analysis of the "hot" to "cold" transition in models with core-mantle feedback. The transition value for $f_\nu = 5.0$, [K] = 200 ppm is equal to $H_0^* = 14.713908672332763672$ TW (black). In green we plot a solution with $H_0 = 14.713908672332763671$, i.e. smaller only by the least numerically tractable difference. (For interpretation of the references to colour in this figure legend, the reader is referred to the web version of this article.)

As is obvious from the ranges of y-axis in Fig. A1, in the coupled models, unlike in the models with a predefined $Q_{CMB}(t)$, the transition solution is not physically acceptable. Its important aspect is that the core's initial temperature reaches hundreds of thousands Kelvin in the backward in time integration. This means that, unlike in the models discussed in Section 3.2, forward in time simulations with reasonable initial conditions do not converge to the transition solution. To recover it, extremely high value of $T_{CMB}(t = -4.5)$ would be needed. This may explain why some authors found backward integration to be numerically unstable and avoided such approach (e.g. Butler and Peltier, 2002).

In the Sections 2.2 and 3.2, transition function $H_0^* = H_0^*(T_m^0, Q_S^0)$ was used to infer the amount of radiogenic heating in the mantle that is consistent with the observations of the present-day mantle temperature T_m^0 and the present-day surface heat flow Q_S^0 (this approach is typical also in the literature). For models with core-mantle feedback, this is no longer the case – a better estimate of H_0 satisfying the constraints given by T_m^0 and Q_S^0 is the best-fit value H_0^f.

In Fig. A2 we perform forward in time simulations for the case with $f_\nu = 5.0$ and [K] = 200 ppm, that is, the same parameters as for the backward in time simulations in Fig. 8. The initial mantle temperature $T_m(-4.5$ Gyr) is varied evenly in the range from 1300 to 3300 K. The amount of present-day internal heating H_0 is $H_0 = H_0^f \approx 16.247$ TW for all the forward simulations. The initial CMB temperature is set to 6430 K, which corresponds to the value obtained in the backward simulation of the best-fit solution (a similar result would be obtained for any $T_{CMB} \sim 10^4$ K). We see that the best-fit solution well represents this class of solutions, similarly as the forward simulations converged to the transition solution in Fig. 2. Note that in Sections 2.2 and 3.2 the transition function $H_0^*(T_m^0, Q_S^0)$ was nearly identical to the best-fit function $H_0^f(T_m^0, Q_S^0)$ and it was not necessary to distinguish between the two.
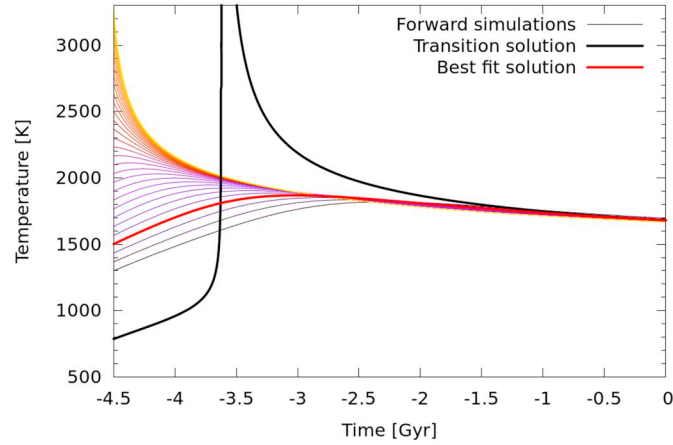
Fig. A2. Similar to Fig. 2. We show 30 forward-in-time simulations, evenly spanning the $\langle 1300, 3300 \rangle$ K range with their initial temperature $T_m(-4.5\,\text{Gyr})$. The viscosity factor f_ν is equal to 5 and $H_0 = H_0^f$ for all the thin colored lines.

Another interesting aspect of the solutions depicted in Fig. 8 of the main text is the range of T_m that is reached at time $t = -4.5$ Gyr. Unlike in Sections 2.2 and 3.2, this range is limited and the function $T_m|_{t=-4.5}(H_0)$ is non-monotonic with respect to changes in H_0. In Fig. A2 we show the $T_m|_{t=-4.5}(H_0)$ relationship for the simulation sets from Figs. 4 and 8 (red and black curves). On the right panel of the figure we show the corresponding values of $T_{\text{CMB}}(-4.5\,\text{Gyr})$. As discussed above, T_{CMB} rises sharply as H_0 approaches H_0^* (red squares), while it is constant in the models of Section 3.2 (but the value of course depends on θ_0 and θ_p).

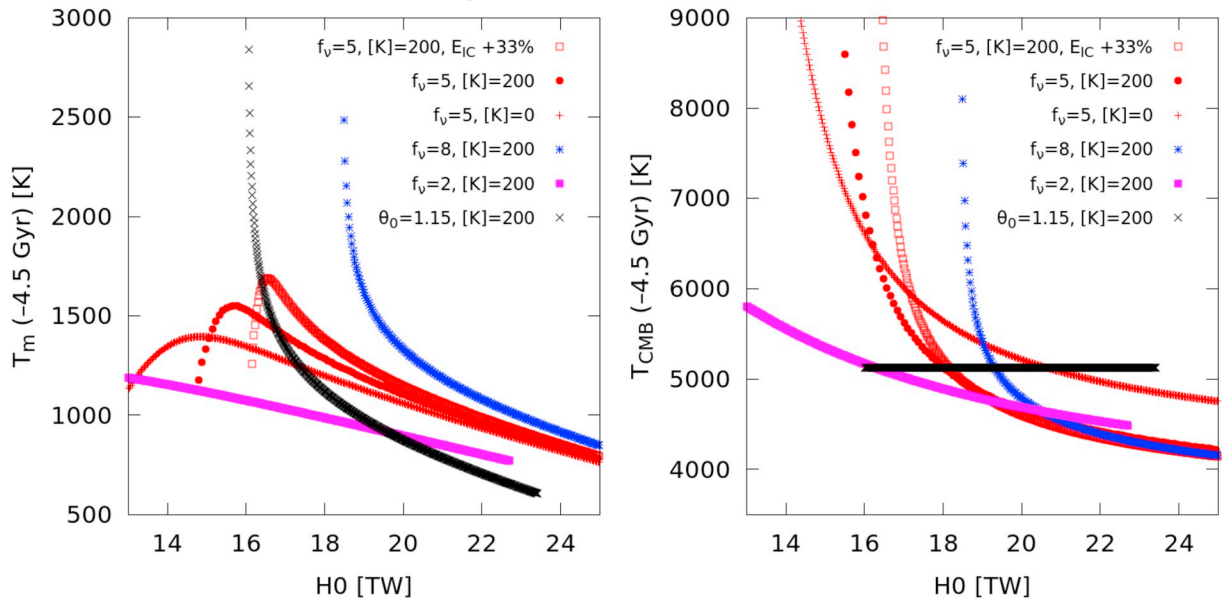**Fig. A3.** Mantle and CMB temperatures at time $t = -4.5$ Gyr for selected best-fit models from Section 3.2 (black, $\theta_0 = \theta_p = 1.15$) and Section 4 (the remaining points). Taking into account radiogenic potassium in the core (red circles) or assuming that a larger energy release accompanies the IC growth (red squares) expands the range of initial mantle temperatures to higher values with respect to the reference model with [K] = 0 (red crosses). (For interpretation of the references to colour in this figure legend, the reader is referred to the web version of this article.)

The rather limited range of $T_m|_{t=-4.5}(H_0)$ observed in Section 4 may seem troubling in view of reconciling Earth's thermal history, as the mantle was likely hotter than 1800 K when it solidified from the primordial magma ocean (see the main text). The range of $T_m|_{t=-4.5}$ depicted in Fig. A3 is $\langle 800, 1600 \rangle$ K, i.e. not containing any temperatures around 1800 K. Also, the obtained range may seem to contradict the results plotted in Fig. A2 (forward and backward integrations of the same equations are just two mathematical approaches that should yield, for given boundary conditions, identical results).

Indeed, there is a problem with the forward simulations shown in Fig. A2. When Q_{CMB} is a function of mantle temperature and not known a priori, the age of IC is not known beforehand either. In the backward simulations we deal with this issue as described in the main text, but in the forward simulations performed here we simply assume IC to start growing when the core's center temperature T_0 reaches the liquidus T_{L0}. This, however, means that nothing ensures that the integral of $Q_{\text{CMB}} - Q_R$ over a_{IC} is equal to the total expected energy E_{IC}, making these forward simulations inconsistent.

This brings us to the role of the energy release accompanying the IC growth, $E_{\text{IC}} = \mathscr{L} + \mathscr{X} + \mathscr{C}$. We employ the value 29.7×10^{28} J referenced in Labrosse (2015), but core energetics are associated with various uncertainties regarding the input parameters. In Fig. A4 we repeat Fig. 8 from the main text, but this time assuming E_{IC} to be 40×10^{28} J, i.e. a value larger by 33%. We see that the upper limit of $T_m(-4.5\,\text{Gyr})$ shifts to a higher value, ca. 1700 K (see also the respective curve in Fig. A3). This means that, for a given viscosity factor f_ν, increasing E_{IC} can result in more realistic mantle temperatures in the Archean.
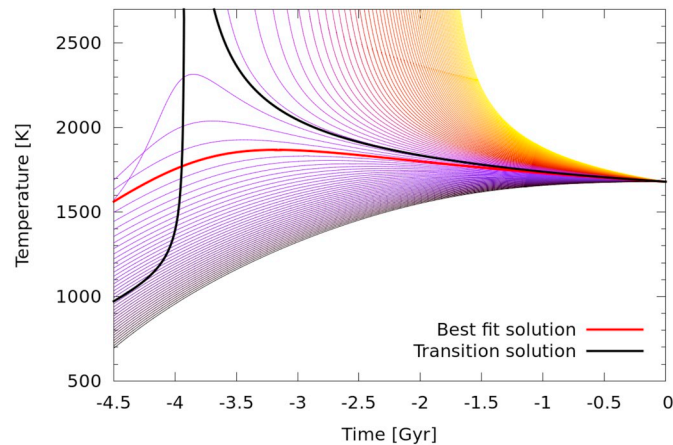
Fig. A4. Same as on the right panel of Fig. 8, only here the energy release associated with IC growth is enlarged, $E_{IC} = 40 \times 10^{28}$ J. The range of $T_m(-4.5 \text{ Gyr})$ is broader in comparison to Fig. 8.

The key parameter controlling the range of $T_m(-4.5 \text{ Gyr})$, however, is the viscosity factor f_ν itself. As shown in Fig. A5, increasing f_ν expands the spectrum of obtained solutions dramatically. This is consistent with the fact that the difference between H_0^* and H_0^f decreases as f_ν increases, and the behaviour of models with $Q_{CMB}(T_m)$ and $Q_{CMB}(\theta_0, \theta_p)$ becomes similar (cf. Fig. 9).
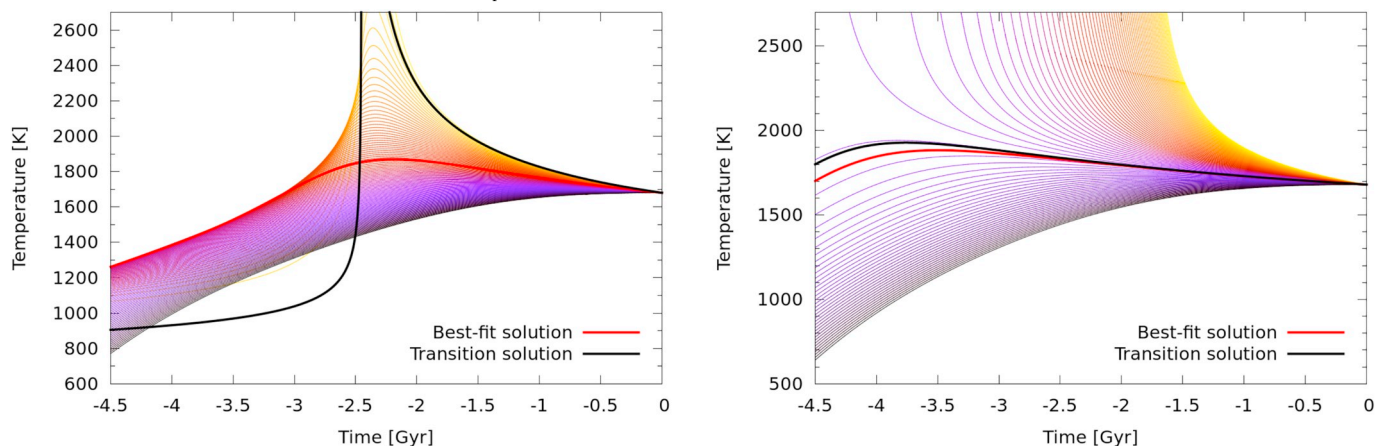

Fig. A5. Same as the right panel of Fig. 8, only $f_\nu = 2.0$ (left) and $f_\nu = 8.0$ (right). For $f_\nu = 2.0$, the transition value H_0^* is close to zero (cf. Fig. 9) and for $f_\nu < 2.0$ the temperature peak (in yellow) would thus completely disappear, along with the concept of transition solution. For $f_\nu = 8.0$, on the other hand, the behaviour of models with $Q_{CMB}(T_m)$ becomes similar to the behaviour of models with a predefined $Q_{CMB}(t)$. (For interpretation of the references to colour in this figure legend, the reader is referred to the web version of this article.)

References

Abbott, D., Burgess, L., Longhi, J., Smith, W., 1994. An empirical thermal history of the earth's upper-mantle. J. Geophys. Res. 99 (B7), 13835–13850.

Agostini, M. et al., 2015. Spectroscopy of geoneutrinos from 2056 days of Borexino data, *Phys. Rev. D*, **92**(3), 031101, Borexino Collaboration, arXiv:1506.04610.

Agrusta, R., Morison, A., Labrosse, S., Deguen, R., Alboussière, T., Tackley, P.J., Dubuffet, F., 2019. Mantle convection interacting with magma oceans. Geophys. J. Int. 220, 1878–1892.

Armann, M., Tackley, P., 2012. Simulating the thermochemical magmatic and tectonic evolution of Venus's mantle and lithosphere: two-dimensional models. J. Geophys. Res. 117.

Armstrong, R., 1991. The persistent myth of crustal growth. Australian J. Earth Sci. 38 (5), 613–630.

Aubert, J., Labrosse, S., Poitou, C., 2009. Modelling the palaeo-evolution of the geodynamo. Geophys. J. Int. 179 (3), 1414–1428.

Badro, J., Aubert, J., Hirose, K., Nomura, R., Blanchard, I., Borensztajn, S., Siebert, J., 2018. Magnesium partitioning between earth's mantle and core and its potential to drive an early exsolution geodynamo. Geophys. Res. Lett. 45 (24), 13,240–13,248.

Bellini, G., Ianni, A., Ludhova, L., Mantovani, F., & McDonough, W. F., 2013. Geo-neutrinos, *Progress Particle Nucl. Phys.*, **73**, 1–34, arXiv:1310.3732.

Belousova, E., Kostitsyn, Y., Griffin, W.L., Begg, G.C., O'Reilly, S.Y., Pearson, N.J., 2010. The growth of the continental crust: constraints from zircon hf-isotope data. Lithos 119 (3–4), 457–466.

Bercovici, D., Ricard, Y., 2005. Tectonic plate generation and two-phase damage: void growth versus grain size reduction. J. Geophys. Res. 110 (B3).

Bono, R. K., Tarduno, J. A., Nimmo, F., & Cottrell, R. D., 2019. Young inner core inferred

from Ediacaran ultra-low geomagnetic field intensity, *Nat. Geo*, **12**(2), 143+.

Booker, J., Stengel, K., 1978. Further thoughts on convective heat-transport in a variable-viscosity fluid. J. Fluid Mech. 86 (MAY), 289–291.

Buffett, B., 2002. Estimates of heat flow in the deep mantle based on the power requirements for the geodynamo. Geophys. Res. Lett. 29 (12).

Butler, S., Peltier, W., 2002. Thermal evolution of earth: models with time-dependent layering of mantle convection which satisfy the Urey ratio constraint. J. Geophys. Res. 107 (B6).

Chidester, B.A., Rahman, Z., Righter, K., Campbell, A.J., 2017. Metal-silicate partitioning of U: implications for the heat budget of the core and evidence for reduced U in the mantle. Geochim. Cosmochim. Acta 199, 1–12.

Christensen, U., 1985. Thermal evolution models for the earth. J. Geophys. Res. **90** (NB4), 2995–3007.

Coltice, N., Rolf, T., Tackley, P.J., Labrosse, S., 2012. Dynamic causes of the relation between area and age of the ocean floor. Science 336 (6079), 335–338.

Conrad, C., Hager, B., 1999. The thermal evolution of an earth with strong subduction zones. Geophys. Res. Lett. 26 (19), 3041–3044.

Cooper, C.M., Lenardic, A., Moresi, L., 2006. Effects of continental insulation and the partitioning of heat producing elements on the earth's heat loss. Geophys. Res. Lett. 33 (13).

Crowley, J.W., O'Connell, R.J., 2012. An analytic model of convection in a system with layered viscosity and plates. Geophys. J. Int. 188 (1), 61–78.

Crowley, J.W., Gérault, M., O'Connell, R.J., 2011. On the relative influence of heat and water transport on planetary dynamics. Earth Planet. Sci. Lett. 310 (3–4), 380–388.

Davies, C.J., 2015. Cooling history of earths core With high thermal conductivity. pepi 247, 65–79.

Davies, G., 1980. Thermal histories of convective earth models and constraints on radiogenic heat-production in the earth. J. Geophys. Res. 85 (NB5), 2517–2530.

Davies, G.F., 2009. Effect of plate bending on the Urey ratio and the thermal evolution of the mantle. Earth Planet. Sci. Lett. 287 (3–4), 513–518.

de Koker, N., Steinle-Neumann, G., Vlcek, V., 2012. Electrical resistivity and thermal conductivity of liquid Fe alloys at high P and T, and heat flux in Earth's core. Proc. Nat. A. Sci. USA 109 (11), 4070–4073.

Deschamps, F., Lin, J., 2014. Stagnant lid convection in 3d-cartesian geometry: scaling laws and applications to icy moons and dwarf planets. Phys. Earth Planet. Inter. 229, 40–54.

Dhuime, B., Hawkesworth, C.J., Cawood, P.A., Storey, C.D., 2012. A change in the geodynamics of continental growth 3 billion years ago. Science 335 (6074), 1334–1336.

Driscoll, P., Bercovici, D., 2014. On the thermal and magnetic histories of earth and venus: influences of melting, radioactivity, and conductivity. Phys. Earth Planet. Inter. 236, 36–51.

Du, Z., Boujibar, A., Driscoll, P., Fei, Y., 2019. Experimental constraints on an MgO ex-solution-driven geodynamo. Geophys. Res. Lett. 46 (13), 7379–7385.

Fowler, A., 1993. Toward a description of convection with temperature-and-pressure-dependent viscosity. Stud. Appl. Math. 88 (2), 113–139.

Gando, A., et al., 2013. Reactor on-off antineutrino measurement with KamLAND. Phys. Rev. D 88 (3), 033001 (KamLAND collaboration, arXiv:1303.4667).

Garnero, E., Helmberger, D., Grand, S., 1993. Constraining outermost core velocity with SmKS waves. Geophys. Res. Lett. 20 (22), 2463–2466.

Gomi, H., Ohta, K., Hirose, K., Labrosse, S., Caracas, R., Verstraete, M.J., Hernlund, J.W., 2013. The high conductivity of iron and thermal evolution of the earth's core. Phys. Earth Planet. Inter. 224, 88–103.

Grigné, C., Labrosse, S., 2001. Effects of continents on earth cooling: thermal blanketing and depletion in radioactive elements. Geophys. Res. Lett. 28, 2707–2710.

Grigne, C., Labrosse, S., Tackley, P., 2005. Convective heat transfer as a function of wavelength: implications for the cooling of the earth. J. Geophys. Res. 110 (B3).

Gurnis, M., 1989. A reassessment of the heat-transport by variable viscosity convection with plates and lids. Geophys. Res. Lett. 16 (2), 179–182.

Helffrich, G., Kaneshima, S., 2010. Outer-core compositional stratification from observed core wave speed profiles. Nature 468 (7325), 807–U96.

Herzberg, C., Condie, K., Korenaga, J., 2010. Thermal history of the earth and its petrological expression. Earth Planet. Sci. Lett. 292 (1–2), 79–88.

Hirose, K., Labrosse, S., Hernlund, J., 2013. Composition and state of the core. In: Jeanloz, R. (Ed.), Ann. Rev. Earth Planet Sci. vol. 41 of Ann. Rev. Earth Planet Sci pp. 657 + .

Hirose, K., Morard, G., Sinmyo, R., Umemoto, K., Hernlund, J., Helffrich, G., Labrosse, S., 2017. Crystallization of silicon dioxide and compositional evolution of the earth's core. Nature 543 (7643), 99–102.

Höink, T., Lenardic, A., 2010. Long wavelength convection, PoiseuilleCouette flow in the low-viscosity asthenosphere and the strength of plate margins. Geophys. J. Int. 180 (1), 23–33.

Höink, T., Lenardic, A., Jellinek, A.M., 2013. Earths thermal evolution with multiple convection modes: a Monte-Carlo approach. Phys. Earth Planet. Inter. 221, 22–26.

Honda, S., 1995. A simple parameterized model of earths thermal history with the transition from layered to whole mantle convection. Earth Planet. Sci. Lett. 131 (3–4), 357–369.

Honda, S., 1997. A possible role of weak zone at plate margin on secular mantle cooling. Geophys. Res. Lett. 24 (22), 2861–2864.

Irving, J.C.E., Cottaar, S., Lekic, V., 2018. Seismically determined elastic parameters for Earth's outer core. Sci. Adv. 4 (6).

Jarvis, G., 1984. Time-dependent convection in the earth's mantle. Phys. Earth Planet. Inter. 36 (3–4), 305–327.

Jaupart, C., Labrosse, S., Lucazeau, F., Mareschal, J., 2015. Temperatures, heat, and energy in the mantle of the Earth. In: Schubert, G. (Ed.), Treatise Geophys. Elsevier, Oxford, pp. 223–270.

Katsura, T., Yamada, H., Shinmei, T., Kubo, A., Ono, S., Kanzaki, M., Yoneda, A., Walter, M., Ito, E., Urakawa, S., Funakoshi, K., Utsumi, W., 2003. Post-spinel transition in Mg2SiO4 determined by high P-T in situ X-ray diffractometry. Phys. Earth Planet. Inter. 136 (1–2), 11–24.

Konôpková, Z., McWilliams, R.S., Gómez-Pérez, N., Goncharov, A.F., 2016. Direct measurement of thermal conductivity in solid iron at planetary core conditions. Nature 534 (7605), 99.

Korenaga, J., 2003. Energetics of mantle convection and the fate of fossil heat. Geophys. Res. Lett. 30 (8).

Korenaga, J., 2008. Urey ratio and the structure and evolution of earth's mantle. Rev. Geophys. 46 (2).

Korenaga, J., 2010. Scaling of plate tectonic convection with pseudoplastic rheology. J. Geophys. Res. 115.

Korenaga, J., 2013. In: Jeanloz, R. (Ed.), Initiation and Evolution of Plate Tectonics on Earth: Theories and Observations. vol. 41 of Ann. Rev. Earth Planet Sci. pp. 117–151.

Labrosse, S., 2015. Thermal evolution of the core with a high thermal conductivity. Phys. Earth Planet. Inter. 247 (SI), 36–55.

Labrosse, S., 2016. Thermal State and Evolution of the Earth Core and Deep Mantle. chap. 4. American Geophysical Union (AGU), pp. 43–54.

Labrosse, S., Jaupart, C., 2007. Thermal evolution of the earth: secular changes and fluctuations of plate characteristics. Earth Planet. Sci. Lett. 260 (3–4), 465–481.

Labrosse, S., Hernlund, J.W., Coltice, N., 2007. A crystallizing dense magma ocean at the base of the earth's mantle. Nature 450 (7171), 866–869.

Litasov, K., Ohtani, E., 2002. Phase relations and melt compositions in CMAS-pyrolite-H2O system up to 25 GPa. Phys. Earth Planet. Inter. 134 (1–2), 105–127.

Lourenco, D.L., Rozel, A.B., Gerya, T., Tackley, P.J., 2018. Efficient cooling of rocky planets by intrusive magmatism. Nat. Geosci. 11 (5) (322 +).

McKenzie, D., Roberts, J., Weiss, N., 1974. Convection in Earth's mantle - towards a numerical simulation. J. Fluid Mech. 62 (FEB11), 465–538.

Megnin, C., Bunge, H., Romanowicz, B., Richards, M., 1997. Imaging 3-D spherical convection models: what can seismic tomography tell us about mantle dynamics? Geophys. Res. Lett. 24 (11), 1299–1302.

Mollett, S., 1984. Thermal and Magnetic Constraints on the Cooling of the Earth. 76. pp. 653–666.

Moresi, L.-N., Solomatov, V., 1995. Numerical investigation of 2d convection with extremely large viscosity variations. Phys. Fluids 7 (9), 2154–2162.

Nakagawa, T., Tackley, P.J., 2005. Deep mantle heat flow and thermal evolution of the earth's core in thermochemical multiphase models of mantle convection. 6, Q08003. https://doi.org/10.1029/2005GC000967.

Nakagawa, T., Tackley, P.J., 2013. Implications of high core thermal conductivity on earth's coupled mantle and core evolution. Geophys. Res. Lett. 40 (11), 2652–2656.

Nisbet, E., Cheadle, M., Arndt, N., Bickle, M., 1993. Constraining the potential temperature of the Archean mantle - a review of the evidence from komatiites. Lithos 30 (3–4), 291–307.

Ohta, K., Kuwayama, Y., Hirose, K., Shimizu, K., Ohishi, Y., 2016. Experimental determination of the electrical resistivity of iron at earths core conditions. Nature 534 (7605), 95.

O'Neill, C., Debaille, V., 2014. The evolution of hadeaneoarchaean geodynamics. Earth Planet. Sci. Lett. 406, 49–58.

O'Rourke, J.G., Stevenson, D.J., 2016. Powering Earth's dynamo with magnesium precipitation from the core. Nature 529, 387.

O'Rourke, J.G., Korenaga, J., Stevenson, D.J., 2017. Thermal evolution of earth with magnesium precipitation in the core, *Earth Planet.* Sci. Lett. 458, 263–272.

Parmentier, E., Turcotte, D., Torrance, K., 1976. Studies of finite-amplitude non-newtonian thermal convection with application to convection in Earth's mantle. J. Geophys. Res. 81 (11), 1839–1846.

Patočka, V., Čížková, H., Tackley, P., 2018. Do elasticity and a free surface affect lithospheric stresses caused by upper-mantle convection? Geophys. J. Int. 216 (3), 1740–1760.

Paulson, A., Zhong, S., Wahr, J., 2005. Modelling post-glacial rebound with lateral viscosity variations. Geophys. J. Int. 163 (1), 357–371.

Poirier, J., 1994. Light-elements in the Earth's outer core - a critical review. Phys. Earth Inter. 85 (3–4), 319–337.

Pozzo, M., Davies, C., Gubbins, D., Alfe, D., 2012. Thermal and electrical conductivity of iron at Earth's core conditions. Nature 485 (7398), 355–U99.

Reese, C., Solomatov, V., Moresi, L.-N., 1998. Heat transport efficiency for stagnant lid convection with dislocation viscosity: application to mars and venus. J. Geophys. Res. 103 (E6), 13643–13657.

Rosas, J.C., Korenaga, J., 2018. Rapid crustal growth and efficient crustal recycling in the early earth: implications for hadean and archean geodynamics. Earth Planet. Sci. Lett. 494, 42–49.

Rossby, H., 1969. A study of Benard convection with and without rotation. J. Fluid Mech. 36, 309–335.

Schubert, G., Anderson, C.A., 1985. Finite element calculations of very high rayleigh number thermal convection. Geophys. J. R. Astron. Soc. 80 (3), 575–601.

Schubert, G., Cassen, P., Young, R., 1979. Subsolidus convective cooling histories of terrestrial planets. Icarus 38 (2), 192–211.

Schubert, G., Stevenson, D., Cassen, P., 1980. Whole planet cooling and the radiogenic heat-source contents of the Earth and Moon. J. Geophys. Res. 85 (NB5), 2531–2538.

Sleep, N., 1990. Hotspots and mantle plumes - some phenomenology. J. Geophys. Res. 95 (B5), 6715–6736.

Sleep, N., 2000. Evolution of the mode of convection within terrestrial planets. J. Geophys. Res. 105 (E7), 17563–17578.

Solomatov, V., 2001. Grain size-dependent viscosity convection and the thermal evolution of the earth. Earth Planet. Sci. Lett. 191 (3–4), 203–212.

Sotin, C., Labrosse, S., 1999. Three-dimensional thermal convection in an iso-viscous, infinite Prandtl number fluid heated from within and from below: applications to the transfer of heat through planetary mantles. Phys. Earth Planet. Inter. 112 (3–4), 171–190.

Stacey, F., 1981. In: O'Connel, R.J. (Ed.), Cooling Earth - a Constraint on Paleotectonic Hypothesis. Geodyn. Ser, vol. 5 of Evolution of the Earth. pp. 272–276.

Stacey, F.D., Anderson, O.L., 2001. Electrical and thermal conductivities of Fe–Ni–Si alloy under core conditions. pepi 124 (3-4), 153–162.

Tackley, P., 1995. On the penetration of an endothermic phase-transition by upwellings and downwellings. J. Geophys. Res. 100 (B8), 15477–15488.

Tanaka, S., 2007. Possibility of a low P-wave velocity layer in the outermost core from global SmKS waveforms. Earth Planet. Sci. Lett. 259 (3–4), 486–499.

Tozer, D.C., 1965. Thermal history of the earth: I. the formation of the core. Geophys. J. Int. 9 (2–3), 95–112.

Turcotte, D., Oxburgh, E., 1967. Finite amplitude convection cells and continental drift. J. Fluid Mech. 28, 29–42.

Turcotte, D., Schubert, G., 2002. Geodynamics. Cambridge University Press.

van der Meer, D.G., Spakman, W., van Hinsbergen, D.J.J., Amaru, M.L., Torsvik, T.H., 2010. Towards absolute plate motions constrained by lower-mantle slab remnants. Nat. Geosci. 3 (1), 36–40.

Williams, Q., 2018. The thermal conductivity of Earth's core: a key geophysical parameter's constraints and uncertainties. Annu. Rev. Earth Planet. Sci. 46 (1), 47–66.

Yamazaki, D., Karato, S., 2001. Some mineral physics constraints on the rheology and geothermal structure of earth's lower mantle. Am. Mineral. 86 (4), 385–391.

Young, R., 1974. Finite-amplitude thermal convection in a spherical-shell. J. Fluid Mech. 63 (MAY15), 695–721.

Yuen, D., Reuteler, D., Balachandar, S., Steinbach, V., Malevsky, A., Smedsmo, J., 1994. Various influences on 3-dimensional mantle convection with phase-transitions. Phys. Earth Planet. Inter. 86 (1–3), 185–203.